

Direct evidence for hydrothermal fluid mineralization in the Velkerri Formation, Northern Australia.

By

Peter Targett

A thesis submitted to Macquarie University
for the degree of Master of Research
Department of Earth and Planetary Sciences
15th of October 2018



MACQUARIE
University
SYDNEY · AUSTRALIA

This work has not previously been submitted for a degree or diploma in any university. To the best of my knowledge and belief, the thesis contains no material previously published or written by another person except where due reference is made in the thesis itself.

(Signed) _____

Date: 15th October 2018 _____

Acknowledgements

The writing of this thesis would not have been possible without the efforts and support of numerous people, and I will attempt to acknowledge those who contributed as best I can. I would first like to thank my supervisor Dr Martin Kennedy. Thank you for your patience and dedication to assisting my project towards completion, weekly philosophical and scientific discussions, and the final few weeks of revision and editing that helped put this thesis together. I would also like to thank Dr Sean Murray for his invaluable knowledge and expertise running Macquarie University's clumped isotope lab, for without his assistance I would not have the quality of data that I had. I would also like to thank Geoscience Australia for the use of their core library, an assistance in selecting analysing samples without which this these could not have been written.

On a personal note, I would like to thank my Parents, Grandparents, and friends at Macquarie University who throughout these two years have treated me with kindness and supported me through difficult times. I would particularly like to thank my Grandparents; Peter and Jill, who's generosity has ensured my time as a student has been as enjoyable and as productive as possible, and to my partner Ailis who's love, and support has been instrumental in getting me over the line. Thank you for your patience and wisdom.

Lastly, to my brother Ian. Writing this thesis has been challenging in many respects, particularly the time that it has taken away from watching you grow up. However, in the little time I have been home these past two years, I have found I have learnt as much from you as I have from my studies. Your boundless energy and infectious curiosity inspire me to tackle scientific research with an open mind, and determination. Academic achievement is something to be proud of, though it is not always synonymous with personal success nor happiness. I look forward to one day seeing how you measure your own success and create your own happiness.

Abstract

The presence of reactive iron and sulfur within marine sediments is routinely used as a proxy for marine anoxia in ancient sediments, assuming these elements were sourced from the overlying water column. Iron and sulfur in sediments of the 1.42 Ga Velkerri Formation in the McArthur Basin, northern Australia serve as one of the key records of Earth's oxygenation history. This thesis shows that much of this iron and sulfur was introduced by hydrothermal fluids long after deposition. Mineralized veins and breccias cut across sedimentary laminae at micro and macro scales. They are composed of vein lining dolomite, ankerite, pyrite, chalcopyrite, quartz, rutile, and iron oxides (hematite and magnesioferrite) indicating multiple fluid generations. Nanometer- scale mineral mapping combined with high resolution electron imaging identifies pervasive influence of later fluids in veins and micro pores through the sediment. 20 – 70% of Fe and S bearing pyrite can be attributed to later fluid sources using this approach, which would go unrecognized using averaged bulk sample analyses attributing this fraction to a seawater source. Clumped isotope palaeothermometry identifies a range of precipitation temperatures; 88.25 – 201.61 °C consistent with hydrothermal mineralization observed throughout the McArthur Basin.

Table of Contents

Acknowledgements	3
Abstract	4
Table of Contents	5
1. Introduction.....	7
1.1 Ocean Chemistry and Redox	7
1.2 Redox Proxies.	9
Trace Element Proxies	10
1.3 The Velkerri formation.	12
1.4 Regional setting and Basin stratigraphy.....	13
1.5 Regional Mineralisation.....	13
1.6 Aim.....	14
2 Methods.....	15
2.1 Samples: Selection.....	15
2.2 Samples: Preparation	15
2.2.1 Cutting:	15
2.2.2 Embedding in Resin:	15
2.2.3 Polishing:	16
2.2.3 Mounting:	16
2.2.4 Ion-Milling:.....	16
2.2.5 Carbon Coating:	16
2.3 SEM-EDX Mineral Mapping (Nano-Min).....	16
2.4 Clumped Isotope Palaeothermometry.....	17
2.4.1 Carbonate Preparation:	17
2.4.2 Sample reaction and cleaning:	17
2.4.3 Data acquisition:.....	18
3. Results	20
3.1 Velkerri Formation in the Urapunga 4 Core	20
3.2 Carbonate Veins.	26
3.2.1 Dolomite-Ankerite Veins.	26
3.2.2 U4 151.58m	27
3.2.4 U4 210.65m	27
3.2.3 Late stage ankerite veins.	28
3.2.6 Iron Oxides.....	29
3.2.5 Late stage dickite fracture fill	29
3.3 Stable and Clumped Isotopes.	29
4. Discussion	48

5. Conclusions.....	55
6. References.....	56
Supplementary Data.....	62

1. Introduction

The oxygenation of Earth's oceans and atmosphere has had irreversible effects on the Earth system and is a necessary condition to support the evolution of complex multicellular life (Lyons *et al.*, 2014). Basic evidence for the accumulation of free oxygen in the atmosphere is the abundance of redox sensitive elements at 2.4 Ga and 2.1 Ga including the disappearance of Banded Iron Formations, the loss of riverine pyrite and uraninite due to oxidative weathering, and the occurrence of rust red soil horizons or 'Red Beds' (Canfield, 2005; Holland, 2006) and mass independent fractionation of sulfur isotopes (Farquhar *et al.*, 2000).

The oceans have had a more complex pathway to the present state of oxidation than the atmosphere. Their oxidation state is influenced by circulation, nutrient availability, restriction and stratification, local biologically related gradients in oxygen (O₂), and partial pressure of free O₂. Given that the dominance of Precambrian life occurred in the oceans, the history of its oxidation is key to understanding the linkage between evolutionary steps and environmental changes leading to complex life (Canfield *et al.*, 2007). This history is constructed from geochemical proxies of elements and minerals that are sensitive to oxidation in ancient sediments (Lyons *et al.*, 2014). Assembling this record is complicated by the limited number of well-preserved geochemical records through the interval of change, their representativeness of the global ocean and the potential for diagenetic alteration of proxies. These challenges have led to controversy surrounding the timing of major changes in oxygen state of the ocean from dissolved iron (ferruginous) to sulfidic, co-existing oxygenated and anoxic portions of the ocean to largely oxygenated state of today (Canfield *et al.*, 1996, 2008, Canfield, 1998, 2005; Poulton *et al.*, 2010).

1.1 Ocean Chemistry and Redox

Iron plays a key role in ocean chemistry (Jenkyns *et al.*, 2006). Iron, depending on the redox chemistry of the oceans, precipitated as pyritic iron (reduced), or iron oxides (oxidized) (Berner, 1984). The preservation of the redox state of iron in sediments is thought to represent the overall redox state of the oceans at the time of precipitation (Raiswell *et al.*, 1988; Lyons *et al.*, 2006). Iron in the oceans significantly affects biological productivity, as a limiting nutrient in the modern oceans (Bekker *et al.*, 2010). Ferric (Fe³⁺) iron is insoluble in oxidizing seawater and highly reactive, precipitating out as iron oxide. In reducing conditions Ferric and Ferrous (Fe²⁺) are soluble, which allows the build-up of iron in reducing water. The occurrence of Banded Iron Formations in the Archean and the Paleoproterozoic is used as evidence that the deep oceans were reducing and

sulfur limited (with the absence of pyrite) due to the high concentrations of ferrous iron until 1.8 Ga (Cloud, 1972). The disappearance of BIFS has therefore been suggested to record the oxygenation of the deep oceans (Cloud, 1972; Holland, 1984). The episodic deposition of BIF's through the Archean Proterozoic Boundary (APB) and Proterozoic would indicate however that widespread oxygenation of the oceans was not consistent nor ubiquitous. Alternatively, BIFs formed on the edges of oases of biologically produced oxygen in an otherwise reducing environment (Anbar *et al.*, 2007).

Canfield proposed a new model for Proterozoic ocean chemistry in 1988. The model hypothesis suggests that oceanic bottom water anoxia persisted through much of the Proterozoic, and that sulfate, not oxygen, was the primary oxidant (Canfield, 1998). This contrasts with the hypothesis that the cessation of BIF formation at 1.8 Ga was a result of the oxidation of Paleoproterozoic bottom waters using oxygen produced by cyanobacteria (Cloud, 1972; Holland *et al.*, 1990). The model is based on shifts in sulfur isotope values implying an increasing concentration of seawater sulfate at around 2.3 Ga (Des Marais *et al.*, 1992) and an increasing rate of sulfide production through sulfate reduction. This excess sulfide is suggested to have counteracted the marine iron flux by 1.8 Ga resulting in the precipitation of reactive iron (as pyrite) and the disappearance of BIF's as a dominant marine sedimentary sequence (Canfield, 1998). Box modelling indicates that either; low atmospheric oxygen and extremely low nutrient availability, or high atmospheric oxygen levels and high nutrient availability is required to develop oxygen enriched ocean waters (Canfield, 1998, Canfield, 2005). This is comparable to the modern ocean which functions with high oxygen and high nutrient availability (Canfield, 1998).

Oxygenation of the atmosphere also causes increased rates of sulfide weathering in the terrestrial environment, driving a greater flux of sulfate to the oceans (Canfield *et al.*, 2007). Increased sulfate content in the oceans lead to an increased sulfate reservoir for bacterial sulfate reduction. Bacterial sulfate produced H_2S interacts with dissolved ferrous (Fe^{2+}) iron, precipitating iron as pyrite as the oceans became increasing sulfidic. The formation of pyrite in marine sediments is therefore interpreted to reflect sulfidic bottom waters (Poulton *et al.*, 2004, 2010).

The Sulfur isotopic record shows little to no fractionation of $^{32}S/^{34}S$ (<10‰) between sedimentary sulfide and sulfate in Archean oceans (Shen *et al.*, 2002). Across the Archean-Proterozoic Boundary, sulfur isotope fractionation increased dramatically to ~40‰ by 2.2 Ga (Strauss *et al.*, 1990; Shen *et al.*, 2002). Significant sulfur fractionation has continued through the remainder of the Earth's history, and the fractionation of sulfur indicates the first accumulation of

seawater sulfate to significant concentrations (D. E. Canfield *et al.*, 2007). Seawater sulfate under anoxic bottom waters is metabolized by bacterial sulfate reducers to H₂S (Berner *et al.*, 1983). Sedimentary sulfide produced by bacterial sulfate reduction are depleted in ³²S relative to the sulfur isotope composition of seawater sulfate (Habicht *et al.*, 1997). Seawater sulfate concentration limits the biogeochemical cycling of sulfur in modern oxygen rich oceans and atmospheres. Therefore, seawater sulfate and sulfur isotope characteristics of ancient sediments can reflect the biogeochemical conditions of past oceans (Shen *et al.*, 2002). The relationship between Iron, Sulfur, and Carbon in sediments is thus commonly used to demonstrate redox conditions of the past ocean.

1.2 Redox Proxies.

A critical challenge for geochemical proxies of depositional conditions is constraining subsequent diagenetic alteration. In respect to applying sedimentary marine proxies, a significant challenge is recognizing when they record the broader oceanic oxygen state, or other processes such as chemical conditions in sedimentary pores influenced by reactive organic matter and concentration of dissolved elements (Canfield, 1989). Pyrite in sediments is widely assumed to form within a closed geochemical system from the initial iron sourced from seawater. While the potential for pyrite formation from diagenetic sources such as basinal fluids, hydrothermal fluids, Fe sources from clay minerals, or hydrocarbon migration is acknowledged, it is rarely explicitly considered.

Mineralogical proxies such as Degree of Pyritization (DOP) have been developed to recognise the degree of bottom – water oxygenation in organic carbon enriched sedimentary rocks (Raiswell *et al.*, 1988). Sedimentary pyrite is a major abiotic sink of ferrous iron in the ancient oceans, and its abundance has been linked to the oxygenation content of the atmosphere and seawater sulfate concentrations (Berner, 1984). Pyrite formation is limited by the supply of sedimentary organic matter, seawater sulfate and reactive iron in detrital minerals (Raiswell *et al.*, 1986; Balci *et al.*, 2007). Freshwater and marine environments experience different limitations due to the limited supply of sulfate in rivers and lakes. The DOP relies on the assumption that seawater sulfate is reduced to H₂S, which reacts with detrital iron minerals and forms as syngenetic or early diagenetic pyrite. Pyrite formed under these conditions by microbial sulfate reduction requires suboxic to euxinic bottom water conditions to be preserved. In oxygenated waters pyrite is readily oxidized (Raiswell *et al.*, 1998). Particularly in Phanerozoic sediments, where oxygenated bottom waters are affected by bioturbation which increases the oxygenation penetration depth. This therefore allows DOP measurements to discriminate euxinic from aerobic sediments, with implications for the

degree of bottom water oxygenation (Raiswell *et al.*, 1988). DOP is measured from 0 – 1, and is defined as:

$$DOP = \frac{\textit{Pyritic Iron}}{(\textit{Pyritic Iron} + \textit{HCl} - \textit{Soluble Fe})}$$

Equation 1: Degree of Pyritization (DOP) as defined by Raiswell et al., (1988)

DOP values > 0.75 represent anoxic or euxinic environments. Values < 0.45 represent oxygenated conditions, and values between 0.45 and 0.75 represent suboxic to euxinic (Raiswell *et al.*, 1988).

The DOP proxy recognises the concentration of organic matter in sediments is necessary for bacterial sulfate reduction of seawater sulfate (Raiswell *et al.*, 1986, 1998). This provides constraints on the accuracy of DOP measurements in organically depleted shales, and in units dominated by high rates of sedimentary deposition. Organically enriched shales are ideal for investigating paleo – environmental conditions as they have high preservation of iron as pyrite (Bernier *et al.*, 1983; Bernier, 1984; Bekker *et al.*, 2004; Lyons *et al.*, 2006). Shales with low organic carbon content show limited pyrite formation because they are carbon limited which lowers DOP measurements independently from bottom water redox state (Lyons *et al.*, 2006).

This was furthered by (Lyons *et al.*, 2006) who combined DOP and the degree of reactive iron to total iron (Fe_R/Fe_{Total}), and total iron to aluminium (Fe_{Total}/Al) to calculate the degree of oxygenation of bottom waters of modern euxinic environments. These authors note that the addition of Fe_R/Fe_{Total} and Fe_{Total}/Al when considering the redox state of bottom water presents a more robust indication of redox conditions in sedimentary sequences that have undergone metamorphism (Lyons *et al.*, 2006). Application of these proxies was conducted predominantly in phanerozoic sedimentary records.

Trace Element Proxies

Molybdenum concentrations and isotope budgets are sensitive to changes in redox conditions (Arnold *et al.*, 2004). In oxygenated water molybdenum forms the inert compound molybdate; MoO_4^{2-} and as a result Mo is the most abundant dissolved transition metal in the modern ocean (Arnold *et al.*, 2004). However, in euxinic basins such as the Black Sea molybdenum is easily removed from solution by reaction with H_2S and accounts for approximately 50% of the annual removal of marine Mo (Arnold *et al.*, 2004). Euxinic sediments are enriched in ^{97}Mo from the fractionation of $^{97/95}Mo$ as compared to oxidized sediments and igneous units. On this basis $^{97/95}Mo$

fractionation within euxinic basins and isotope mass balancing have been used to track the evolution of seawater redox in ancient marine sediments (Arnold *et al.*, 2004).

Rhenium and osmium exhibit conservative behaviour within modern oceans that is similar to molybdenum (Anbar *et al.*, 1992). Enrichment of Re and Os in sediments correlates primarily with the sedimentation of organic matter and, to a lesser degree, pyrite precipitating under reducing conditions (Creaser *et al.*, 2002; Tribovillard *et al.*, 2003) and can occur concurrently with precipitation of Molybdenum. Therefore, Re-Os and Mo systematics have been used as indicators of post depositional mobilisation and as indicators for diagenetic alteration.

Rhenium-Osmium dating of two stratigraphic units of the Roper group produces robust isochrons in the Velkerri Formation but not the Wollgorang formation implying post depositional remobilisation of Re, Os and Mo in the Wollgorang Formation (Kendall *et al.*, 2009). The Velkerri Formation in the Urapunga – 4 core produces two robust Re/Os isochrons interpreted to represent a depositional age of 1361Ma +/- 21 Ma and 1417 Ma +/- 29 Ma (Kendall *et al.*, 2009). The Wollgorang formation shows a similar age of deposition of 1359ma +/- 150 Ma though with increased scatter about the isochron. This scatter has been attributed to the diagenetic remobilization of Re-Os by hydrothermal fluids related to the nearby McArthur river “Here’s Your Chance” (HYC) sedimentary exhalative deposit (SEDEX) (Chen *et al.*, 2003; Kendall *et al.*, 2009; Spinks *et al.*, 2016). Nearby Settlement Creek and Gold Creek igneous intrusions are hypothesized to be the source of mineralizing fluids (Cooke *et al.*, 1998; Kendall *et al.*, 2009). The Velkerri formation in Urapunga – 4 however, is considered to be unaffected by fluids due to more robust isochrons.

One of the key records used as evidence for the critical interval spanning the shift from ferruginous to sulfidic and partly oxygenated seas in the Mesoproterozoic Velkerri Formation in the southern McArthur Basin (T. H. Donnelly *et al.*, 1988). Geochemical and mineralogical redox proxies have been applied to the sediments of the Velkerri Formation primarily in the Urapunga – 4 core to characterise redox changes in the Mesoproterozoic oceans. These sediments offer a preferred record because; (1) they are composed of a substantial portion of fine-grained pelagic, laminated, semi continuous sediments which record the water column processes and do not show evidence for re-sedimentation (Sweet *et al.*, 1986; T H Donnelly *et al.*, 1988; T. H. Donnelly *et al.*, 1988). (2) Sediments were deposited in a marine environment and are inferred to represent the global ocean (Jackson *et al.*, 1991; Shen *et al.*, 2002). (3) They are thermally immature, minimally folded, and have experienced little tectonism or alteration by intrusive events (Abbott *et al.*, 2000). (4) The Velkerri

formation is organically enriched in two intervals, and thus useful for DOP, $^{97/95}\text{Mo}$, $\text{Fe}_{\text{HR}}/\text{Fe}_{\text{Total}}$ determination (Shen *et al.*, 2003; Kendall *et al.*, 2009).

1.3 The Velkerri formation.

The Velkerri formation is conformable flat lying, 200-370m thick sedimentary sequence and since its deposition has undergone minimal tectonic deformation (Jackson *et al.*, 1987). The Velkerri formation is composed of fine to very fine – grained laminated, stratified, and organically enriched shale (T. H. Donnelly *et al.*, 1988; Jackson *et al.*, 1991; J. E. Gillott *et al.*, 2002). Sediments are subdivided into three lithologically distinct packages; The Upper, Middle and Lower Members. The Velkerri formation is of particular interest to petroleum exploration industries and paleoenvironmental studies due to its significant organic enrichment and the presence of live oil as identified by (Jackson *et al.*, 1986) in the Urapunga – 4 core. The unit contains uncommonly high TOC% values for a Precambrian formation; with 1-3% TOC as a RockEval average, exceeding 5%TOC in three intervals with a maximum 8.7% TOC (Jackson *et al.*, 1991; Warren *et al.*, 1998; Shen *et al.*, 2002). Through the use of vitrinite reflectance proxies (R_o), organic geochemistry indicates low thermal maturity in a well preserved sedimentary sequence as a consequence of shallow burial (Jackson *et al.*, 1991; Warren *et al.*, 1998; Kendall *et al.*, 2009).

The Urapunga – 4 core was drilled as a research well to understand the subsurface stratigraphy of the poorly outcropping McArthur basin. Hydrocarbon and mineral exploration wells were drilled within the Roper basin. Urapunga – 4 was recovered with the best preserved and most continuous stratigraphy of the Roper group sediments (Sweet *et al.*, 1986; Abbott *et al.*, 2001).

Sulfur isotope studies conducted by Shen *et al.*, (2003) record $\sim 40\text{‰}$ shift in $\delta^{34}\text{S}$ isotopic values in the upper Velkerri Formation in the Urapunga – 4 core. Shen *et al.*, (2003) calculated DOP and $\text{Fe}_{\text{HR}}/\text{Fe}_{\text{Total}}$ within the Urapunga – 4 and 5, and Golden Grove stratigraphic cores. They applied DOP to show anoxia in the deep basin facies (> 0.45) (Shen *et al.*, 2003). DOP values decrease to < 0.45 - < 0.34 in sediments interpreted as inner shelf sediments. $\text{Fe}_{\text{HR}}/\text{Fe}_{\text{Total}}$ values record a similar trend (> 0.38 in basinal sediments - < 0.18 in shelf sediments) with paleo gradient shifts (Shen *et al.*, 2003). Systematic fractionation of sulfur isotopes of approximately $\sim 40\text{‰}$ $\delta^{34}\text{S}$ are associated with DOP and $\text{Fe}_{\text{HR}}/\text{Fe}_{\text{Total}}$ defined paleogradient depth. This is supported by evidence for pyrites forming in deep water anoxic sediments which have significantly enriched $\delta^{34}\text{S}$ values (Muir *et al.*, 1985). This evidence has been used to support the hypothesis for stratified Mesoproterozoic oceans (Shen *et al.*, 2003; Kah *et al.*, 2004; Jenkyns *et al.*, 2006).

1.4 Regional setting and Basin stratigraphy.

The Velkerri Formation is within the Roper Group in the Palaeo-Mesoproterozoic McArthur basin (Australian Northern Territory) which covers an area of approximately 180,000km². The Roper Group consists of alternating formations of quartz arenite (10-300m thick) and siltstone and shale (100-300m thick) (T H Donnelly *et al.*, 1988; Jackson *et al.*, 1991; J. E. Gillott *et al.*, 2002). The Roper Group it is markedly different from the underlying carbonate rich groups and is characterized by much more uniform facies deposited in a more stable marine setting. Minimum age of deposition is given by K-Ar dating of dolerite sills that intrude the upper part of the group (McDougall *et al.*, 1965). This was later revised by (Abbott *et al.*, 2001) who gave a SHRIMP U – Pb Baddeleyite age of 1324 +/- 4 Ma. The oldest Rb-Sr age measured on glauconite samples from near the base of the group is the 1390ma +/- 20ma (McDougall *et al.*, 1965). A 1429 +/- 31 ma Rb-Sr date from Illite (separated from carbonate) from the McMinn Formation is interpreted as the maximum age of sedimentation of the McArthur Basin sequence (Kralik, 1982).

The McArthur basin is composed of up to 10km of late Proterozoic and early Mesoproterozoic sedimentary rocks deposited in a fluctuating intra-cratonic marine basin (T. H. Donnelly *et al.*, 1988). Evidence of stromatolites, evaporites, fine siltstones, and very fine mudstones indicate a range of marine depositional environments (Rawlings, 1999). The McArthur basin is dominated by two large fault zones; the north trending Batten fault Zone, and the west trending Urapunga fault zone (Jackson *et al.*, 1987). The basin unconformably lies above Paleoproterozoic Pine Creek, Murphy, and Arnhem provinces, and contacts the Mt Isa Superbasin in its south eastern extent (Ahmad *et al.*, 2013). The Southern McArthur basin is composed of four distinct sedimentary packages; the Tawallah, McArthur, Nathan and Roper groups in depositional order. The younger Roper group was likely deposited in a separate basin to its older counterparts due to its distinct structural setting and sedimentary composition (Sweet *et al.*, 1986; Rawlings, 1999; Abbott *et al.*, 2001). The understanding of sediments is based on material extracted from stratigraphic and mineral exploration wells (Sweet *et al.*, 1986). The basin has been modelled as several north-trending asymmetric rifts, separated by northwest trending faults and transverse ridges. The north trending Batten Fault Zone (BFZ) and the Walker Fault Zone (WFZ) are intersected by the east trending Urapunga Fault Zone (UFZ) as described by (Rawlings, 1999).

1.5 Regional Mineralization

The Southern McArthur shows regional mineralization and contains large economic resources such as the McArthur River HYC deposit which forms a part of the Carpentaria Zinc Belt.

The McArthur River deposit is one of the world's largest Zn – Pb – Cu mine and has had been investigated regarding its emplacement and paragenesis. Mineralization within the McArthur river region is associated with the circulation of fluids through the Batten Fault Zone. Mineralizing fluids were low temperature, saline basinal brines which are associated with regional extension of the basin, and the Settlement creek and Gold creek igneous intrusions (Cooke *et al.*, 1998; Garven *et al.*, 2001). The timing of mineralization has been contentious, with both a syngenetic and post depositional origin hypotheses being suggested (Rye *et al.*, 1981; Eldridge *et al.*, 1993; Garven *et al.*, 2001). U-Pb series date of 1690 +/- 30ma from the Barney Creek Formation is interpreted to be the maximum mineralization age of the McArthur River deposit (Page 1981). U-Pb dates are measured on zircons from tuffs in the mineralized HYC pyritic shale member. A Rb-Sr date of 1589 +/- 28ma (Kralik, 1982) was measured on illite from tuffs in the same member; and a Rb-Sr date of 1537 +/- 52ma (Kralik, 1982) on illite from dolomitic shales above the tuffs. These ages conform to the accepted timing of deposition; ~1590ma – 1700ma, and close to the age of the host sediments of the Mt Isa Pb-Zn deposit which has been correlated with the McArthur group (Plumb *et al.*, 1981).

Other mineralized areas and fluid enrichments include the Mt Vizard Copper prospect (Abbott *et al.*, 2001), Tawallah group base metal sulfides (Cooke *et al.*, 1998), and hydrocarbon migration within the Wollongorang and Velkerri Formations (Flannery *et al.*, 2014; Spinks *et al.*, 2016). The Velkerri Formation is considered unmineralized, and unaffected by migrating basinal fluids (CITATION).

1.6 Aim

This aim of this work is to determine the effect of hydrothermal fluids at the microscale, textural features identified using Back Scattered Electron Microscopy (BSEM) with elemental distribution determined by Energy Dispersive X-ray Spectroscopy (EDX) and mineral composition determined by Nanomin software constraining the observable and microscale extent of mineralization affecting redox sensitive minerals used in seawater proxies. This thesis will present a detailed petrographic description of primary sedimentary features, diagenetic alteration, and to identify if post depositional alteration has affected the Urapunga – 4 core.

2 Methods

Using novel integration of Field Emission Scanning Electron Microscopy (FE-SEM) with mineral mapping using EDX spectroscopy through an integrated system allowing nanoscale mineral quantification identifies the pervasive influence of later fluids in micro pores throughout the Urapunga – 4 core. During core logging as part of this study a series of conspicuous cross cutting mineralized veins were identified at the visual scale. High resolution imaging of minerals within these veins was conducted to determine overall composition and paragenesis.

2.1 Samples: Selection

For this study, samples from the Velkerri Formation (drill core BMR Urapunga-4) were obtained from the drill core library of geoscience Australia in Canberra, ACT. The Urapunga 4 core was analyzed in hand sample from depths 41.91m – 376m. This sample range covers the Upper (42.35m-117.3m), Middle (118.3m-363.7m), and Lower (363.98m-372.45m) Velkerri Formations, as well as the base of the overlying Moroak Sandstone (40.15m-42.35m), and the top of the underlying Bessie Creek Sandstone (372.6m-376m) (Figure 1). From the selected intervals, 21 samples were selected showing evidence of vein like intrusions or hydrothermal ore development. Samples were identified with a hand lens and ranged from sub-millimeter to centimeter scale zones of alteration.

2.2 Samples: Preparation

2.2.1 Cutting:

Samples were cut perpendicular to bedding planes using a diamond saw at a slow speed, using water or ethanol as a lubricant. Ethanol was used for clay rich samples to reduce suction and prevent hydration of swelling clays. Swelling clays are problematic for the preparation process as they eject out of samples upon contact with water, even in heavily lithified samples. This changes the mineral composition of the samples as well as producing micro scratches along sample surface, compromising the competency of the sample. Samples were embedded in resin using 25mm and 30mm diameter resin molds. 30mm diameter resin molds are the preferred diameter for the FEI-SEM Teneo sample stage as the 25mm diameter molds require adaptors to be properly mounted. (if preparing stubs, skip to 2.2.3).

2.2.2 Embedding in Resin:

Samples were placed in polyethylene molds analysis-side down, centered, and labelled. EpoFix™ Cold-Setting Embedding Resin was used to set samples in blocks. EpoFix™ was mixed in a fume cupboard using resin and hardener at a ratio of 8:1, then stirred gently for 2 minutes avoiding

entrainment of air. Once thoroughly mixed, resin is poured over the sample so that it is entirely covered, then left to set for 8 hours in the fume cupboard.

2.2.3 Polishing:

Blocks were first manually polished using diamond grit paper lubricated with either distilled water or 95% ethanol. Polishing was done over four 3 – 4 minute intervals with grit size decreasing in each succeeding stage (400, 600, 800, 1200 grit sizes). Samples were polished until little to no visible scratches or grooves remained. Samples were left to dry overnight before ion-milling. The polishing intensity varied depending on sample integrity. Clay-rich samples were often fragile and brittle requiring the use of ethanol as a lubricant and gentle polishing post-embedding. Harder more metalliferous samples such as those from the center of alteration veins were polished before and after embedding to produce a smoother finish.

2.2.3 Mounting:

Polished sample blocks are mounted on circular pins with an araldite glue and left to set. Once set, samples are ready for ion milling.

2.2.4 Ion-Milling:

Embedded samples were placed in a Hitachi IM4000 Argon Ion Mill system for 30 minutes, at an incident angle of 5° to produce the cleanest polish without risk of scratching the sample through plucking. The samples were mounted onto a stage using carbon tape. A discharge voltage of 1.2V – 1.4V was used with an acceleration voltage of 4.0V – 5.0V. Care was taken to restrict the acceleration voltage and length of sample runs to prevent burning the sample or reacting any volatiles.

2.2.5 Carbon Coating:

Samples were coated with carbon to enhance conductivity of the surface of the samples and enhance SEM imaging. A Carbon coating was chosen over gold or other typical metal coats to reduce the dampening effect on the production of X-rays for energy dispersive X-ray spectroscopy (EDS).

** Thin sections were prepared at Macquarie University Rock Lab. Thin sections are ~100 microns thick, ion milled and carbon coated, as per steps 2.2.4, and 2.2.5 before imaging.

2.3 SEM-EDX Mineral Mapping (Nano-Min)

Carbon coated samples were then imaged using FEI Teneo Field Emission Scanning Electron Microscope (FE-SEM) (Macquarie University) which is equipped with secondary and backscattered-electron detectors and an integrated Bruker energy dispersive X-ray spectroscopy (EDX; Bruker

XFlash Series 6) analyzer. Quantitative identification of mineral and surface imaging was investigated at acceleration voltages between 15 and 20kV. Mineral mapping was performed using the FEI maps mineralogy software and the Nanomin system. Mineral abundance is determined by the Nanomin system using EDX data collected at 500nm pixel resolution. The peak intensities are compared to an extensive mineral library and up to three mineral phases are modeled for each pixel. The accuracy of the Nanomin mineral identification can be independently established by comparing the mineral boundaries assigned by Nanomin to the underlying BSEM image in which the mineral outlines are evident. The direct overlap of these boundaries is evident in figure 5 providing confidence that Nanomin can accurately identify pyrite. Nanomin combines X-ray spectral analyses pixel by pixel over high resolution backscatter textural images. By correlating X-ray spectra and mineral textures, the mineral composition of samples can be calculated as an area percentage. This style of micro scale analysis allows for rapid, and accurate determination of minerals phases and their associations. Nanomin is designed specifically for fine-grained sediments, such as shales to enable deconvolution and identification of potential minerals that form mixed phase X-ray spectra. Using this method, a paragenetic history of the sample was determined through classification of primary, diagenetic and metasomatic alteration events.

2.4 Clumped Isotope Palaeothermometry

Clumped isotope palaeothermometry was used to determine the isotopic composition of CO₂ gases and the range of temperatures of the precipitating carbonate fluids.

2.4.1 Carbonate Preparation:

Dolomite (CaMg(CO₃)₂) veins were drilled using a benchtop foot powered microdrill taking care to reduce contamination by not drilling through to other layers. Commonly, 10-20 mg of sample was acquired from each vein.

2.4.2 Sample reaction and cleaning:

A single clumped isotope sample consisted of 4mg-6mg of pure carbonate material placed into a two-legged man glass reaction vessel. After sample addition, the side-leg was half-filled with 105% phosphoric acid (H₃PO₄) and then evacuated on a vacuum line to ~10⁻⁴ atm. The samples were subsequently placed into a 90°C water bath and the acid allowed to equilibrate for 30 minutes before reaction. Dolomite samples were reacted for ≥60 minutes until no visible evidence of reaction (bubbles in the acid) were present. A carbonate standard was reacted and measured every day prior to measuring samples to check the functioning of the mass spectrometer. These carbonates were only reacted for ~25 minutes.

After reaction, the two-legged men were attached to an in-house stainless-steel vacuum line specifically designed to produce clumped isotope samples. The product CO₂ was collected using a Dewar of liquid N₂ on a U-trap. Once all bubbles in the phosphoric acid of the sample vessel had dissipated, the two-legged-man vessel was sealed. The length of the vacuum line actively being used at this point was then briefly exposed to a roughing pump (Adixen – Pascal 2005 SD) to remove any non-condensable gases. The U-trap containing the sample CO₂ was then sealed off using a Swagelok bellows valve (SS-6BK), and the LN₂ on the U-trap was replaced with a -80°C ethyl-alcohol Dewar and the product CO₂ released while trapping any water produced during the reaction. This CO₂ was then separated from the trapped water using an adjoining U-trap with LN₂ and sealed off from the water-trap using another bellows sealed valve. From here, the CO₂ was released again and allowed to passively diffuse through a Poropak (Type-Q) U-trap with silver-wool caps on each end at -60°C. This low of a temperature was required to clean the large levels of sulfurous contaminants contained in some of the samples (Davies and John, 2016). The CO₂ was recollected using LN₂ in a U-trap past the Poropak-trap. Typically, this stage took ~2 hrs and was allowed to continue until capacitance manometer gauges monitoring the vacuum line returned to baseline. Once completed, the Poropak-trap was sealed off using a bellows-sealed valve, and the CO₂ was then trapped into a glass L-vessel using LN₂, sealed, then removed and placed onto the mass spectrometer. Subsequently, the entire vacuum line was baked at ~150°C for at least one-hour before the next sample was placed onto it (Defliese *et al.*, 2015; Murray *et al.*, 2016).

2.4.3 Data acquisition:

Cleaned CO₂ samples were measured on a ThermoFisher MAT 253-plus mass spectrometer. Samples were analyzed in bellows-mode at 16V on mass 44 against an in-house working gas ($\delta^{13}\text{C} = -6.62\text{‰}$, $\delta^{18}\text{O} = -13.92\text{‰}$ VPDB) calibrated against NBS-19. Samples were measured over 8-blocks with 7 cycles of sample-reference comparison in each block. Data reduction and normalization for the raw Δ_{47} value followed the methods outlined in Huntington *et al.* (2009) except for ¹⁷O correction which was updated to the correction factor described in Brand *et al.* (2010) based on recommendations in Schauer *et al.* (2016) and Daëron *et al.* (2016). The raw Δ_{47} value was translated to the universal reference frame detailed in Dennis *et al.* (2011) using a suite of standard CO₂ gases either heated to 1000°C or equilibrated with water at 25°C, 50°C, or 90°C. The final reported Δ_{47} values were adjusted for the acid fractionation of carbonate reaction at 90°C by +0.083‰ (Murray *et al.*, 2016). Contamination in samples was monitored using the 49-parameter (Davies and Johns, 2017) and excesses in the Δ_{48} value. While some samples reported show evidence of high level of contamination, similarities in Δ_{47} values between contaminated and uncontaminated samples was

taken as evidence for minimal influence on the Δ_{47} value, though discretion was taken with interpreting too much based on this evidence.

The $\delta^{13}\text{C}$ and $\delta^{18}\text{O}$ values were simultaneously measured with the clumped isotope Δ_{47} value. The reported values were calculated following the methods laid out in Gonfiantini et al. (1993) and are relative to Vienna Pee Dee Belemnite (VPDB). The $\delta^{18}\text{O}$ of the dolomite samples were adjusted by -0.8‰ to adjust for the difference in acid fractionation of calcite and dolomite reacted at 90°C (Land, 1980).

The processed Δ_{47} values were converted to temperature using the calibration of Bonifacie et al. (2017). The $\delta^{18}\text{O}$ value of the precipitating fluid was calculated using the calibration of Matthews and Katz (1977) based on the recommendations of Murray et al. (2017) and reported relative to Vienna standard mean ocean water (VSMOW).

3. Results

3.1 Velkerri Formation in the Urapunga 4 Core

The Velkerri Formation is comprised of three lithologically distinct members (Figure 1). The Lower Member unconformably overlies the Bessie Creek Sandstone and is composed of 8.5 metres of laminated and ripple cross laminated silt to fine-grained sandstone that fines upward into organic carbon rich (120-220m and 320-360m) laminated mudstone. This unit is silica cemented and most brittle in the high TOC intervals. TOC declines in the upper portion of the Middle Member as silt content increases into a silty, glauconitic fine sandstone, and slumped beds of the Upper Member. The Middle Member in the U4 core has received the most focus by geologists because of its high TOC, which reaches a peak 11.5% TOC at ~136m (Figure 1). The Middle Velkerri Fm. shows a second distinct TOC peak of 6.2% between ~324 metres and ~326 metres (Figure 1). The middle member lacks evidence of current reworking; such as ripples or scours, indicating the dominance of pelagic deposition with limited reworking. This contrasts with the ripples, graded beds, slumps, fine-sand and silt laminations present in the Upper and Lower members, suggesting influence by bottom currents or intermittent storm influence (Figure 1, 3). Overall the Velkerri Formation shows little interruption from deposition of fine-grained sediments suggesting continuous, deeper-water depositional environment with the finest grained, lowest energy and possibly slowest sedimentation rate in the Middle Member.

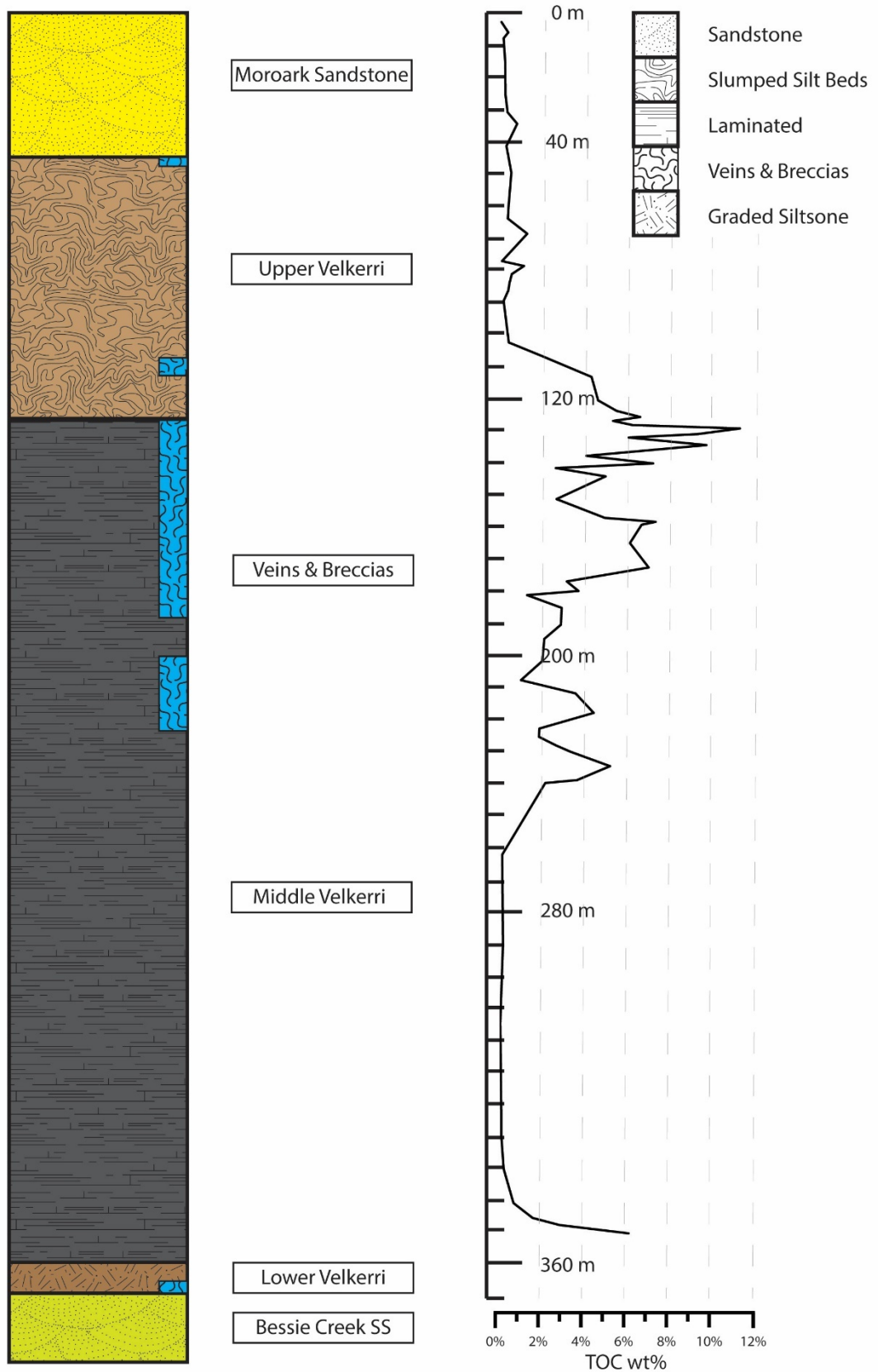


Figure 1: Stratigraphic log of Urapunga – 4. Light blue irregularly lined intervals indicate locations along core where veins were identified. TOC wt% measured on bulk samples (Kennedy et al., unpublished).

The Velkerri Formation shows little post depositional structural alteration, with the exception of the conspicuous series of cross cutting veins filled by dolomite and pyrite In the Urapunga 4 core (Figure 4). There are 80 locations where cross cutting hydrothermal veins and alteration zones were identified between 42.04m and 372.45m. Veins range in thickness from millimeter scale to ~10cm. Breccia zones were observed in multiple locations and are cross cut by later veins (Figure 2). Brecciated intervals exhibit fluid-assisted ‘crackle break’ textures at the visible scale (Figure 2). Mineral composition of cross cutting veins determined by BSE and EDX. Microscale examples of similar mineralization are associated with hydrothermal fluids is evident in samples without conspicuous veins (Figure 9, 14, 15, 16 and 20). Microscale mineralization exhibit similar stratigraphic layering of diagenetic mineral phases (Figure 20). This has been used as evidence for pervasive fluid flow through the Urapunga – 4 core. in The Lower Velkerri Formation U4 core is in places shattered, and veins were difficult to detect lower than 230m. Cross cutting veins occur within all members but is most concentrated in the silicified and organic carbon rich Middle Member. Veins and brecciated domains were imaged and examined using BSE and EDX, and detailed mineral maps were created using mineral mapping software *Nanomin*.



Figure 2: Examples of breccias within Urapunga - 4 core. Breccias exhibit crackle break textures, and show evidence of multiple cross cutting veins.

Pyrite is conspicuous throughout the Middle Member and occurs in a variety of morphologies reflecting different origins. Millimeter – centimeter scale euhedral pyrite aggregates are evident to the naked eye throughout all three members of the Velkerri Formation (Figure 3). Aggregates are roughly spherical and shale laminae thin over these intervals implying formation prior to burial compaction and thus likely formed during early diagenesis near the sea bed. Pyrite also occur at the micron scale as euhedral crystals as either isolated crystals, or within groups of individual euhedral crystals. Isolated euhedral pyrite crystals are dispersed throughout the matrix—and are most commonly ~ 15 microns with rare examples < 5 microns and > 20 microns. Euhedral pyrite crystals can be dispersed through the sediment, but also often are found in clusters or linear arrays following fractures that are sub-parallel to sedimentary laminae and are filled by pyrobitumen. These pyrites are almost always associated with 10-micron apatite spheres that are also filled by pyrobitumen. Rare small (< 5 micron) chalcopyrite crystals also associated with these clusters. All pyrite crystals observed in this study were euhedral in morphology, there were no framboidal or rounded transitional morphologies. Late stage hydrothermal pyrite occurring in cross cutting fractures occurs throughout the silicified Middle Member and is described below.



Figure 3: Pyrite nodules at ~ 110m in Urapunga – 4. Top; nodule is ~1cm in diameter, and shows sediment draping textures. Bottom; nodules are < 0.5cm, and show draping textures.



Figure 4: Orange stickers indicate where veins are observed within the Urapunga 4 core between 166.7m and 170.47m

The Velkerri Formation is an active hydrocarbon system (Jackson *et al.*, 1986) with evidence of both migrated (pyrobitumen) and *insitu* kerogen. Pyrobitumen in U-4 is recognized within (1) stringers that cut across sedimentary laminae at high angles and have branches forming thin tendrils that extend across laminae and could not have been detrital fragments and are unlikely mats. (2) amorphous material filling porosity between detrital and diagenetic chlorite, euhedral pyrite and clay minerals that does not have boundaries defining detrital fragments, (3) filling the interior shelter porosity of later stage apatite spheres (Figure 14 C, D). Kerogen shows distinct grain boundaries where it occurs as fragments and does not cross cut sedimentary laminae where it may have formed as a microbial mat within or at the top of the sediment (Figure 9: *ii*). Microbial mats formed in the benthic environment or deposited from settling pelagic mats could comprise a component of the organic matter in these sediments. Density differences in BSE analysis utilized here do not reveal differences in organic matter compositions, and there can be some ambiguity about migrated versus *insitu* organic matter in specific cases (Milliken *et al.*, 2014).

The structure and distribution of minerals within U-4 indicate some detrital but a dominance of diagenetic phase. The mineralogy of detrital grains within the Middle Velkerri Formation is dominated by quartz, feldspar and mica. Detrital phases are recognized by their sharp grain boundaries and larger grain size in comparison to the diffusive, pore filling diagenetic Illite-smectite and micro-crystalline quartz. Detrital quartz and feldspars are disseminated throughout the Middle Velkerri as isolated silt sized grains of size 20 - 50 microns. Mica flakes up to 60 microns are also randomly dispersed and deposited subparallel to sedimentary bedding (Figure 9).

Diagenetic minerals comprise the bulk of the sediment matrix and are recognized by submicron grain size, occurrence within pores, radiating crystal orientations unrelated to sedimentary laminae, intergrowths and lack of defined boundaries. Dominant pore filling textures include micro quartz crystal ~ 1-micron intergrown with Illite – smectite crystals that can comprise up to 60% of the sediment (Figure 14 – A, *ii*, B, *i*), the majority of the matrix. Quartz micron crystals are distributed as aggregates of < 1-micron crystals that fill open porosity along with apatite, pyrite, and organic matter.

Diagenetic sulfides are dispersed through the matrix filling pores. Chalcopyrite and sphalerite are key diagnostic minerals for the presence of diagenetic mineralization. Examples of chalcopyrite and sphalerite crystals within the sedimentary matrix are shown in (Figure 6).

Detrital grains within the matrix show evidence for diagenetic replacement. The dominant replacement mineral is kaolinite, which also occurs randomly distributed throughout the sedimentary matrix growing as “books” in pores. Kaolinite also occur as 20 micron “books” interlayered with < 2-micron illite – smectite as identified by EDX (Figure 11: A, B, D). these kaolinite books are an order of magnitude larger than surrounding sediments and have well preserved layering. They are tabular in shape, and are of similar size (~20 – 30 microns) to chloritized detrital micas. It is therefore likely that kaolinite in sedimentary matrix is a late stage feature produced by feldspar dissolution and replacement by kaolinite (Figure 11).

3.2 Carbonate Veins.

The Urupunga - 4 core contains approximately 80 post-depositional hydrothermal alteration zones identified between 42.04m and 372.45m as veins, or clusters of veins at the visual scale. Veins and brecciated domains were imaged and examined using BSEM and EDX, and detailed mineral maps were created using mineral mapping system *Nanomin*. BSEM and EDX identify veins filled by iron-magnesium rich carbonates (dolomite – ankerite) which host iron (pyrite) and copper rich sulfides (chalcopyrite), iron-magnesium-titanium oxides and a range of diagenetic silicate minerals. Imaging of carbonates reveals a complex history with multiple fluid events, and changes in mineral precipitation.

3.2.1 Dolomite-Ankerite Veins.

Dolomite ($\text{CaMg}(\text{CO}_3)_2$) is the dominant carbonate phase identified by EDX and is often associated with ankerite ($\text{Ca}(\text{Fe},\text{Mg},\text{Mn})(\text{CO}_3)_2$). Dolomite is predominantly found filling veins which cross cut sedimentary laminations at a low to high angle (Figure 7). Ankerite in these veins lines cavities occurring on an insider layer of dolomite. These Dolomite-Ankerite veins are irregularly shaped, have sharp boundaries. Dolomite-ankerite vein fills have a large size range in cross section from ~100 to >1000 microns (Figure 19). However, in hand sample some 1cm veins, that are subparallel to bedding, are filled by dolo-spar. Dolomite and Ankerite are indistinguishable in hand sample. Dolomite-Ankerite also fills cavities, that extend away from veins and wedge-out within adjacent host rock (Figure 12). The irregular discontinuous shapes and sometimes isolated distribution of branched veins indicate a three-dimensional geometry intersecting the drill core. Sharp, jagged and irregular margins also suggest the opening of fractures from brittle failure likely caused by hydraulic fracturing. Fluid over-pressured is a hypothesized mechanism for the fracture style and fill.

Within dolomite-ankerite veins are significant quantities of euhedral pyrite, and to a lesser extent chalcopyrite. These sulfide minerals occur as euhedral, ‘cauliflower’ shaped crystal aggregates filling

the centre of veins and are dispersed throughout larger dolomite domains (> 1 cm veins) (Figure 7). In larger dolomite domains euhedral pyrite ranges in size from > 50 microns to > 1000 microns (Figure 19). Cauliflower pyrite is always hosted within dolomite and has sharp contact boundaries with ankerite rims. Similarly, euhedral chalcopyrite aggregates are contained only within dolomite. Using BSEM imaging alone, chalcopyrite and pyrite are indistinguishable. EDX analysis identifies a consistent copper peak, which combined with the Nanomin mineral mapping system has been used to identify the mineral as chalcopyrite. However, unlike pyrite, euhedral cauliflower chalcopyrite occurs in a limited number of samples, within a specific depth range. Sample 161.25m (Figure 7) contains the largest individual chalcopyrite crystal aggregate identified, which is approximately 50 microns wide. Dolomite hosted chalcopyrite has also been identified in sample U4 151.58m.

3.2.2 U4 151.58m

Sample U4 151.58m is unique among samples identified. The sample is 10cm long, composed primarily of sulfide minerals and carbonate layers. In hand sample the core section is gold in colour and contains only remnants of the host shale rock within it. BSE and EDX analysis show a core completely dominated by pyrite, with minor accessory chalcopyrite. Dolomite is again the dominant carbonate phase, with some ankerite cavity linings present. In U4 151.58m pyrite is euhedral, cauliflower shaped and occurs in a 'striped' pattern across the sample cross section (Figure 19). By area, pyrite composes approximately 40% of the sample area. Pyrite 'stripes' occur as long (> 800 micron), narrow (< 200 micron) cauliflower shaped aggregates. Host/country rock in U4 151.58m is fragmented and heavily kaolinized. Fragments of country rock are dispersed between dolomite encased pyrite stripes. Fragments are < 50 microns in diameter. Isolated chalcopyrite crystals approximately 25 -30 microns in diameter are associated with euhedral pyrite (Figure 19). Clumped isotope thermometry was not conducted on this sample, due to the high sulfur compound content leading to S contamination during mass spectrometry.

3.2.4 U4 210.65m

Sample U4 210.65-.75m (Figure 17) is heavily altered section of the Urapunga 4 core. The sample is brecciated, approximately 10cm in core length, dominantly grey-white in colour with a silvery sheen and contains visible < 5mm veins throughout. This sample was cut into 5 segments and imaged using BSE and EDX. This imaging reveals a complex diagenetic history, with multiple mineralogically distinct domains. Dolomite-ankerite are the dominant carbonate minerals comprising veins. Siderite (FeCO_3) is identified using EDX and has a similar cavity lining morphology to ankerite. Identified within these samples are heavily chloritized domains that show evidence for brecciation at the

micron scale (Figure 17 – A, B, D). These domains are composed primarily of diagenetic chlorite, pyrite, rutile and apatite with minor diagenetic quartz and are cross cut by dolomite. These domains form as cavity lining structures that separate dolomite that initially formed on the sedimentary matrix (Figure 17 – A, B, D). These diagenetic minerals are commonly of hydrothermal origin where they form as (1) alteration aureoles formed by contact metasomatism, or (2) evidence for earlier hydrothermal fluids of a different chemical composition to the fluids which precipitated dolomite-ankerite and euhedral pyrite. Chloritized domains do not occur in the majority of samples, and clumped isotope thermometry conducted on sample U4 210.65m is not anomalous (116.5 °C) compared with the range of temperatures measured. It is therefore less likely to be a result of contact metasomatism, and more likely evidence for a multiphase hydrothermal fluid system with varying geochemistry.

3.2.3 Late stage ankerite veins.

Ankerite also constitutes later stage veins that cross cut earlier dolomite filled veins, indicating multiple fracturing events. These later-stage, fine scale fractures (< 50-micron: width) cut across existing dolomite-ankerite filled veins *at high angles*. In some samples euhedral pyrites within the early veins are fractured and coated by ankerite where later stage veins intersect them (Figure 5). These fractures have developed *insitu* fragmentation textures (mosaic breccias) in a jigsaw puzzle pattern (Jebrak, 1997) (Figure 5; (A) and (B)). Fragments show little to no rotation of fragments, except in the centre of the largest (~50 micron) veins (Figure 5: C, D). Fragments of the fractured pyrite are contained within the ankerite veins, with some fragments showing jigsaw like pieces, indicated that they have remained closely in place after breakage. Fracture geometry suggests hydraulic fracturing, and rotated fragments are evidence for local scale critical failure (Jebrak, 1997). Fragments and fractures have angular, and sharp boundaries. Late stage ankerite veins mimic the shape of fractured pyrite, replicating angular mineral boundaries in zoned growth 'rings' within fractures. Fragments of pyrite range from 2 – 30 microns in diameter, are angular and have sharp boundaries with ankerite.

Cross cutting fractures lined by ankerite are also spatially associated with goethite, magnesioferrite and dickite. These iron-magnesium oxides and phyllosilicates occur as single crystals, or as rims (Figure: 14 A, *i*). Within dolomite – ankerite, and late stage ankerite veins are sharply bounded kaolinized domains. These regions are homogenous, composed entirely of dickite. This indicates that late stage fluids were depleted in carbonate, rich in silica, and possibly sourcing iron from dissolved pyrite.

3.2.6 Iron Oxides

Iron oxides are associated with diagenetic carbonates as described above. Iron oxides have also been identified filling fractures in the absence of diagenetic carbonates (Figure 15: A, B). These oxides are ~100 microns in diameter and have sharp crystal boundaries with the sedimentary matrix (Figure 15: A, B). Oxides also occur as detrital grains.

3.2.5 Late stage dickite fracture fill

Dickite is identified by BSE and EDX in fractures within dolomite veins and filling fractures breaching the host shale facies. Dickite is also identified within the sediments of the Velkerri Formation and exhibits a different morphology. This second style of dickite is detailed in section 3.3. Within vein fractures and wedge out structures, Dickite occurs in clusters of archetypal 'books'; 2 – 5 microns wide, and up to 15 microns tall. Clusters are tightly packed, showing face to edge contacts, and have defined sharp boundaries. Dickite is the dominant mineral phase where they occur. In cross section, these clusters are 50- 60 microns in width, and up to 200 microns in length. In some samples, there is evidence for Dickite intruding into the host rock, replacing mineral grains at the boundary of dolomite veins. Dickite also fills the tail end of fractures intruding into the host shale, forming a wedge at the end of dolomite veins (Figure 12). The presence of Dickite in fractures within dolomite veins confirms that the hydraulic fracturing occurred as multiple events, and that each event precipitated a chemically distinct mineral assemblage.

Associated with late stage silica fluids is diagenetic quartz cementation. Diagenetic quartz is identified by its cross-cutting relationship with dolomite – ankerite mineralization and euhedral crystal shape. Diagenetic quartz fills porosity within dolomite – ankerite (Figure 10: A) and fills fractures within the sedimentary matrix (Figure 10: B). The sharply defined crystal boundaries of quartz crystals indicate that they are authigenic.

3.3 Stable and Clumped Isotopes.

Dolomite - ankerite veins identified by SEM and EDX were sample and analyzed for their stable isotopic composition. Stable and clumped isotope data are presented in table 1. Data has been adjusted to account for sample contamination of $\delta^{13}\text{C}$. $\delta^{13}\text{C}$ values show variation within replicate analyses, with up to a 2‰ shift across samples associated with contamination. Variation in $\delta^{13}\text{C}$ values was compared against standards measured to account for drift. Standard measurements show < 0.2‰ variation across sample dates. Calibrating for this does not account for the large variability of $\delta^{13}\text{C}$ values in dolomite samples. Corrected $\delta^{13}\text{C}$ data has a range of -2.53 to 38.62 (Table 1). $\delta^{18}\text{O}$ values with better reproducibility of < 1‰ across all samples. The $\delta^{18}\text{O}$ of the

dolomite samples were adjusted by -0.8‰ to account for the difference in acid fractionation of calcite and dolomite reacted at 90°C (Lynton S. Land, 1980; Murray *et al.*, 2016). All carbon and oxygen isotopic compositions are reported relative to VDPB (Vienna Pee Dee Belemnite). $\delta^{18}\text{O}$ values range from -9.6 to -14.2‰. $\delta^{13}\text{C}$ values range from -2.5 to -38.7.

The carbonate clumped isotope measurement is made on CO_2 derived from calcium-magnesium carbonate and measures the abundances of CO_2 molecules that have both ^{13}C and ^{18}O ($^{13}\text{C}^{16}\text{O}^{18}\text{O}$ = mass of 47). This is described by the Δ_{47} parameter (Dennis, 2011). Unlike traditional stable isotope measurements, clumped isotope measurements are susceptible to isobaric interference from a wider range of contaminants, including hydrocarbons, and sulfur compounds (Eiler, 2011). The error reported for Δ_{47} is based on internal error of standards. This technique measures the degree of clumping of heavy isotopes of carbon and oxygen in the carbonate lattice in comparison with a random distribution. The degree of clumping; expressed as Δ_{47} in units of permil shows a systematic dependence of temperature (Dennis, 2011). Δ_{47} values are corrected for acid fractionation effects as per (Murray *et al.*, 2016). Variation in Δ_{48} values is interpreted to be recording contamination from non – condensable gases passing through the Porapak trap (Petersen *et al.*, 2016). Similarly Δ_{49} values reported are relative measures of sample contamination (Davies *et al.*, 2017). Sample contamination was expected based on the high organic content of the unit, and heavy sulfide mineralization within dolomite – ankerite veins. Application of dolomite clumped isotope thermometry to these materials provides constraints on their origin and diagenetic history. High resolution imaging of veins indicate that contained within carbonate minerals are assemblages of iron – sulfide minerals. Therefore, it was expected that error about the Δ_{48} and Δ_{49} parameter would be evident in the data.

Table 1: Stable and Clumped isotope data. Fluid temperatures calibrated for Bonifacie et al., (2017)

Sample Depth	U4 210.65m	U4 146.76m	U4 161.25m	U4 142.2m	U4 152.4m	U4 155.7m	U4 158.5m	U4 225.5m	U4 377.7m
$\delta^{13}\text{C}$ (VPDB)	-9.21	-10.35	-10.85	-5.16	-7.23	-10.70	-2.53	-10.79	-38.62
Std. Dev.	0.02	0.02	0.02	0.02	0.02	0.01	0.01	0.01	0.02
Std. Er.	0.00	0.00	0.00	0.00	0.00	0.00	0.00	0.00	0.00
$\delta^{18}\text{O}$ (VPDB)	-13.19	-13.44	-13.11	-12.03	-12.25	-13.25	-11.54	-13.37	-8.79
$\delta^{18}\text{O}$ (dolomite)	-13.99	-14.24	-13.91	-12.83	-13.05	-14.05	-12.34	-14.17	-9.59
Std. Dev.	0.00	0.01	0.08	0.03	0.03	0.01	0.01	0.02	0.09
Std. Er.	-2.30	-3.39	0.01	0.00	0.00	0.00	0.00	0.00	0.01
$\delta 47$	0.08	0.09	-5.45	1.19	-1.04	-5.46	3.85	-5.78	-28.14
$\Delta 47$	0.06	0.08	-0.50	-0.50	-0.50	-0.51	-0.47	-0.63	-0.54
Std. Dev.	0.01	0.02	0.11	0.05	0.06	0.07	0.07	0.07	0.11
Std. Er.	166.66	759.42	0.01	0.01	0.01	0.01	0.01	0.01	0.01
$\Delta 48$	8.48	25.61	9.92	27.30	0.63	363.71	0.27	1.11	1.21
Std. Dev.	1.13	5.59	0.49	0.92	0.25	12.52	0.41	0.37	0.31
Std. Er.	-8.47	-132.64	0.07	0.12	0.04	1.67	0.06	0.05	0.04
$\Delta 49$	4.46	5.31	25.75	-6.29	-4.20	-48.22	-14.01	18.97	26.42
Std. Dev.	0.60	1.16	6.15	4.11	2.99	8.49	8.59	6.68	4.61
Reaction Temp	90.00	90.00	90.00	90.00	90.00	90.00	90.00	90.00	90.00
49 Parameter	-0.86	-8.12	1.03	-0.29	-0.23	-3.47	-0.62	0.99	-0.06
Fluid Temp	116.45	94.95	121.96	140.82	133.47	123.07	88.25	201.61	95.18

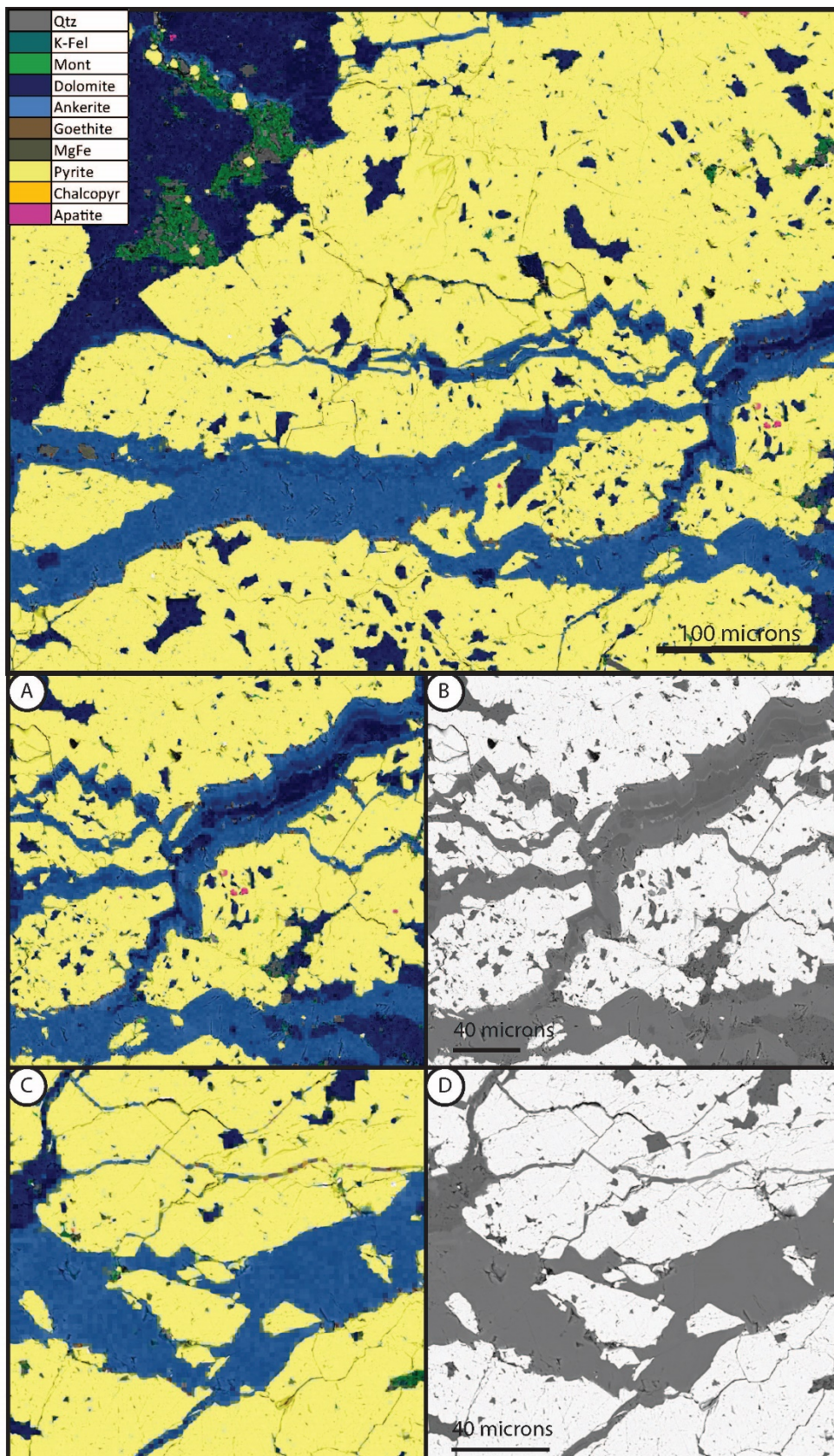


Figure 5: Brecciated diagenetic pyrite. Late stage ankerite veins cross cut earlier dolomite – ankerite veins and euhedral pyrite aggregates. Brecciation caused fragments to break off into vein centres. Jigsaw like fractures indicate fragments remained together, and sharp boundaries indicate minimal dissolution of surfaces.

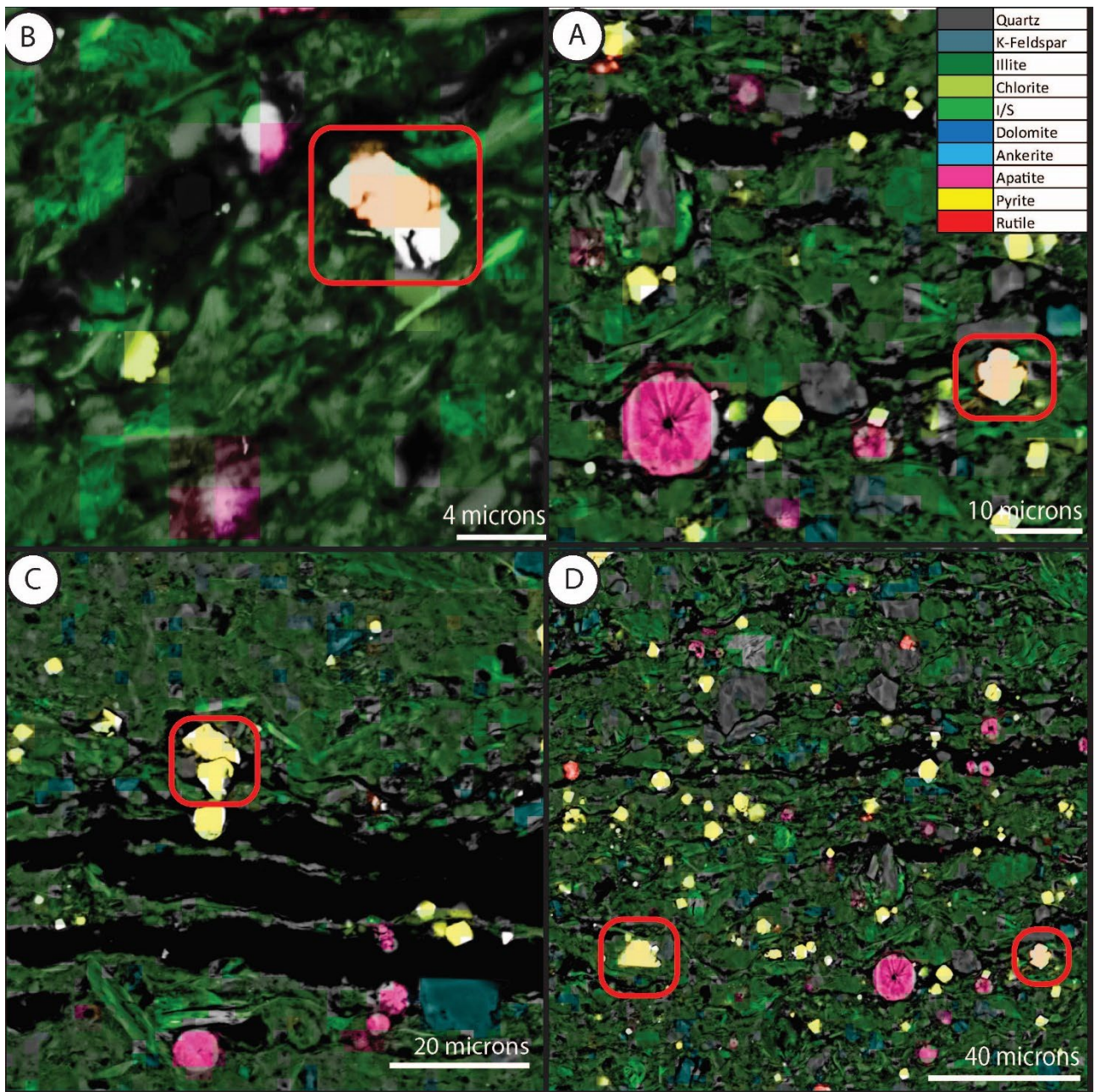


Figure 6: Diagenetic chalcopyrite and sphalerite crystals within sedimentary matrix. (A): sample depth 161.25m, (B, C, D) sample depth 136.00m. (C) Highlight in red are sphalerite crystals with a copper peak, potentially indicating remineralization to chalcopyrite. (D) highlighted in red from left to right; Euhedral sphalerite crystal ~ 10 microns wide, and euhedral chalcopyrite crystal ~ 5 microns wide. Sedimentary matrix composed primarily of quartz – illite (< 1 microns), Illite/smectite (~ 5 microns), euhedral pyrite (< 5 microns - ~ 10 microns), ‘solid’ apatite spheres, and K-Feldspar. Accessory rutile and chlorite.

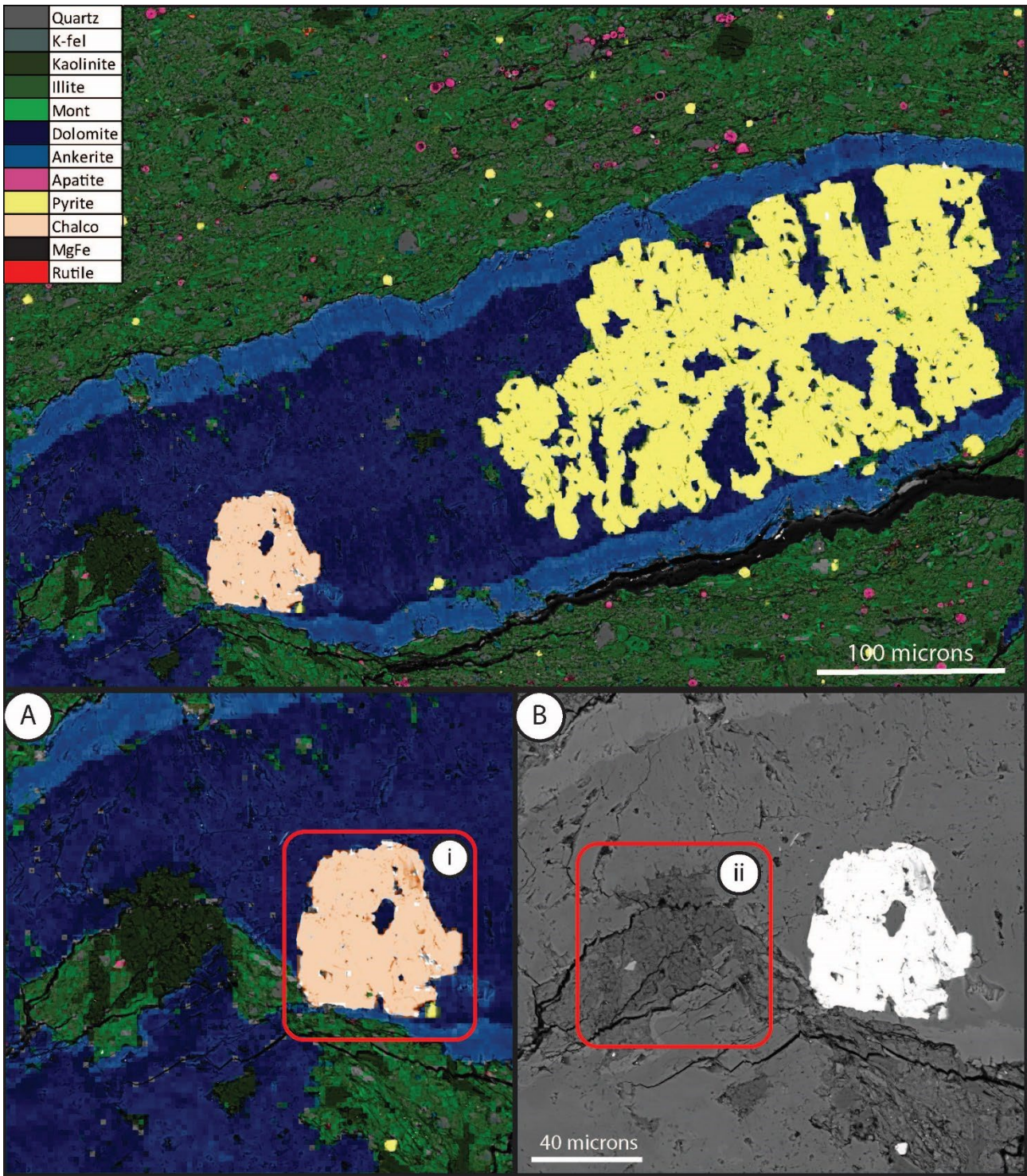


Figure 7: Cross cutting dolomite – ankerite vein at 161.25m in U4 core. Hosted within carbonate phases are; euhedral pyrite cauliflower aggregates ~ 200 microns in length, (A, i) Euhedral chalcopyrite ~ 50 microns in diameter, and (B,i) fracture filling kaolinite or dickite clusters. Sedimentary matrix of sample identified as quartz – illite (< 1 microns), montmorillonite (illite/smectite interlayer), euhedral pyrite and apatite spheres associated with fractures, and recrystallised detrital quartz, accessory K-Feldspar, rutile and Mg/Fe oxides.

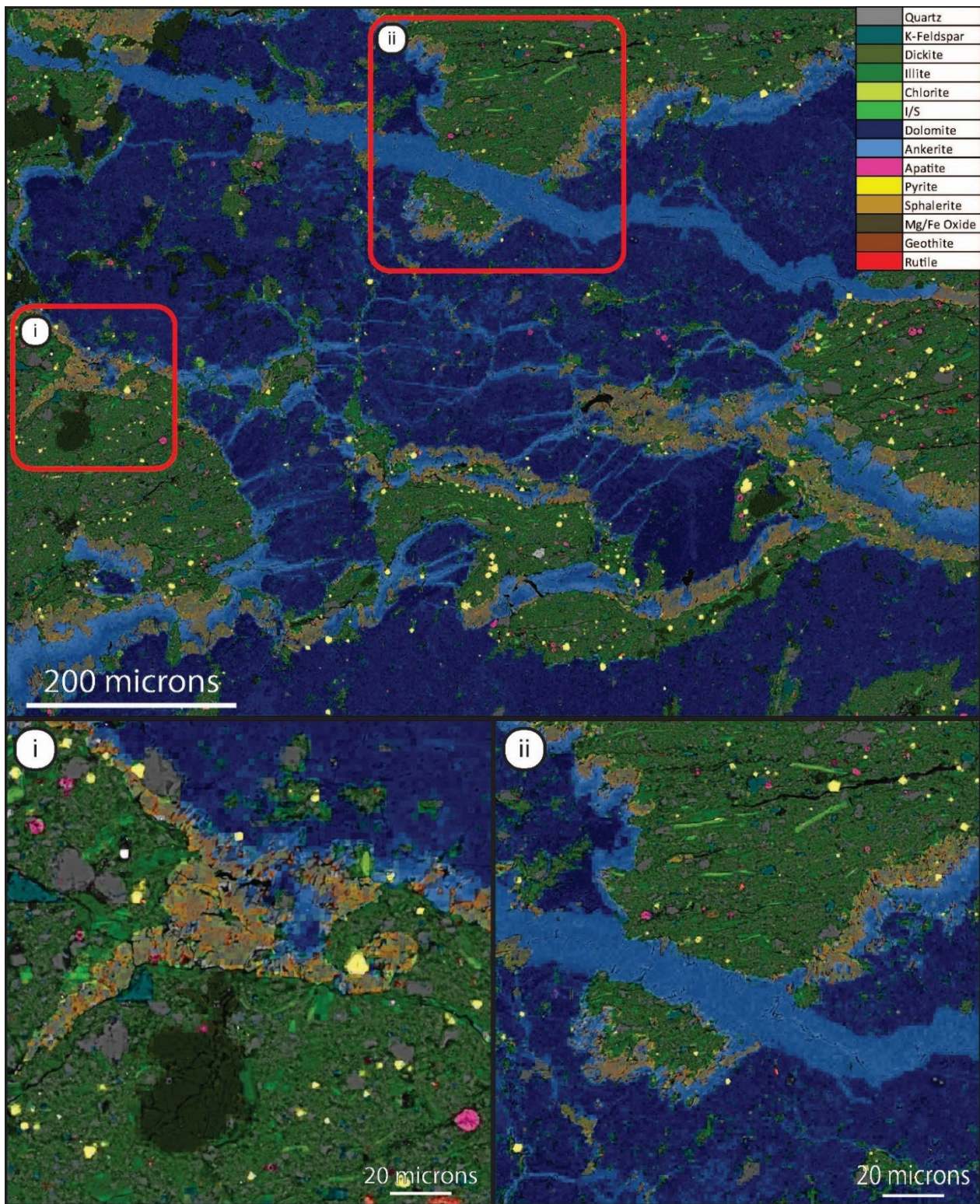


Figure 8: Late stage Ankerite veins (144m) cutting across earlier diagenetic dolomite and fractured sedimentary matrix (ii). Late stage ankerite closely associated with Fe-Mg rich iron oxides. Oxides are randomly distributed throughout late stage veins, and fill porosity within dolomite. Oxides penetrate sedimentary matrix through fractures (i) and line contact between matrix and intruding ankerite veins (ii). Hosted within dolomite phases are diagenetic sulfides; pyrite (yellow) and sphalerite (Orange). Diagenetic kaolinite or dickite (dark green) precipitated in porosity created by fracturing within dolomite – ankerite veins. Kaolinite or Dickite also occurs within sedimentary matrix (i). Mineral map above illustrates multiple generations of compositionally distinct fluids.

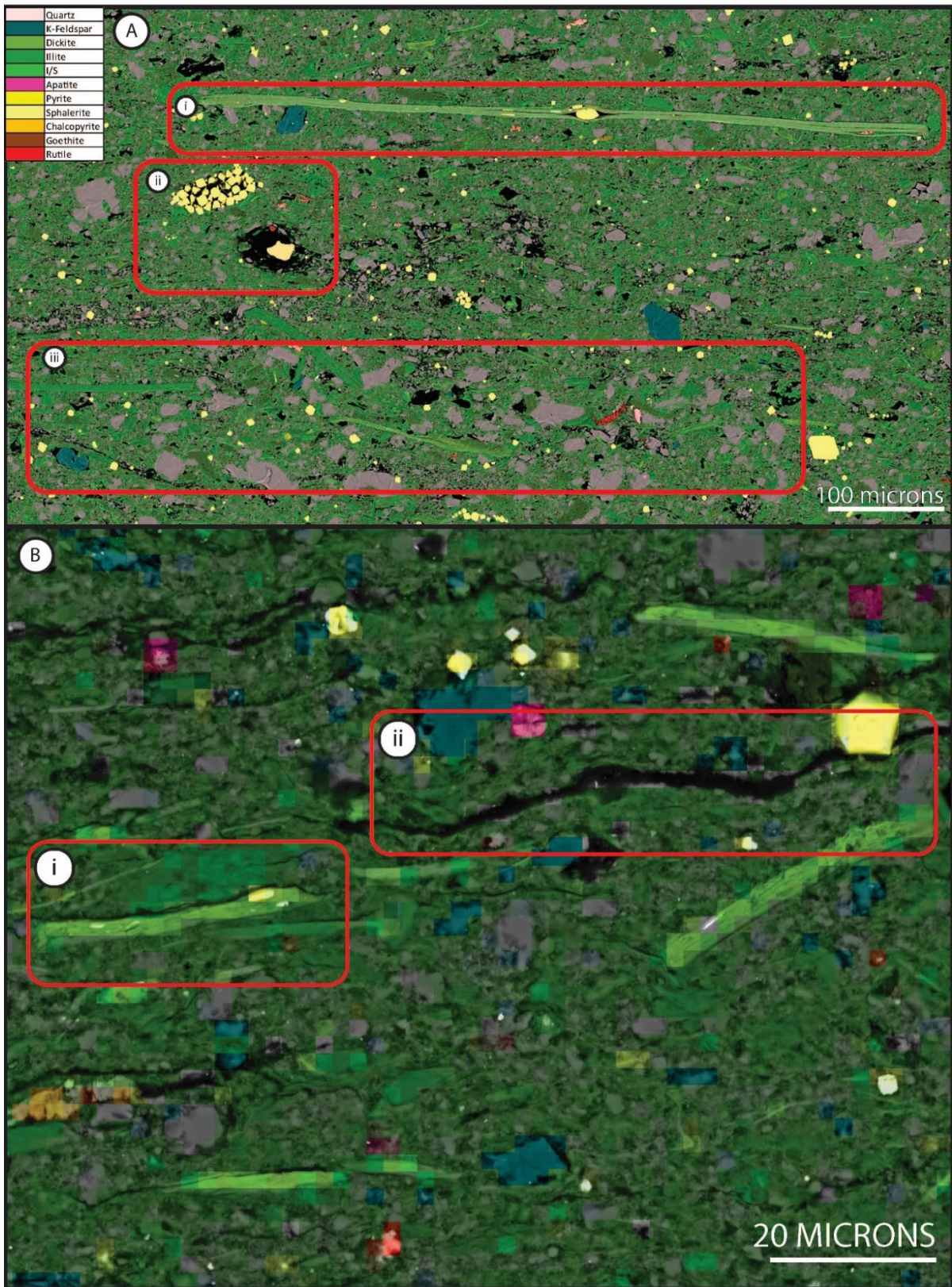


Figure 9: Top Image (A) sample depth 326m, Bottom image (B) sample depth 144m. Detrital grains in diagenetic matrix (bright green) and range in size from 20 - 400 microns A (i). Detrital grains in figure are interpreted as mica flakes, which have been diagenetically remineralized to chlorite. B (ii) Organic stringer within sedimentary matrix. A (ii), and (iii) contain diagenetic pyrite, sphalerite and rutile associated with hydrothermal fluids. A (iii) grain size and stratigraphy of quartz indicates detrital origin.

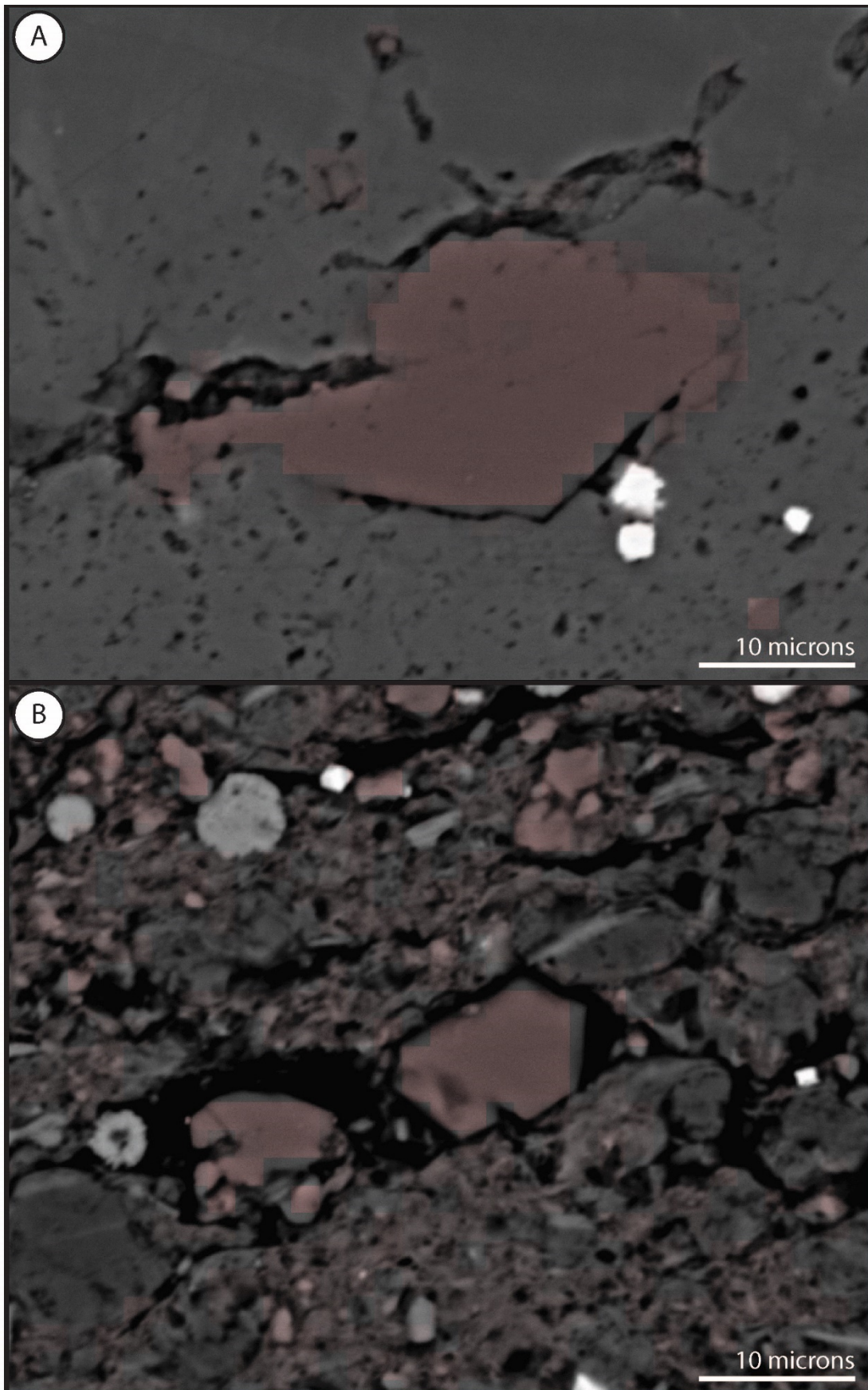


Figure 10: (A) 30-micron euhedral diagenetic quartz crystal within cross cutting dolomite vein. (B) 10-micron euhedral diagenetic quartz within fracture – Hexagonal. Sample depths 151.58m

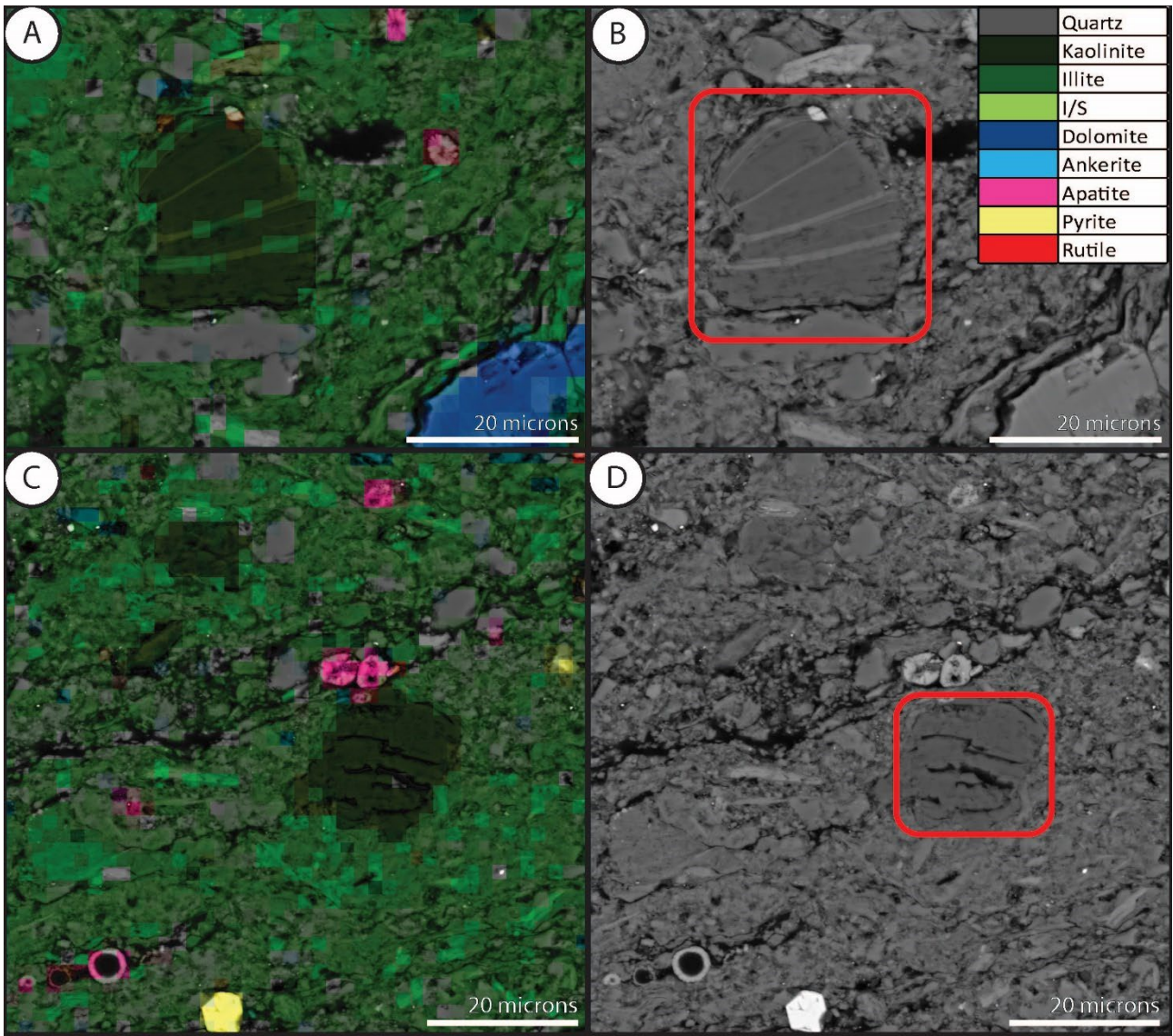


Figure 11: Kaolinite replacement of detrital grains. Replacement kaolinite is either; (A, B) interlayered with illite clay crystals, or (C, D) as pure kaolinite books.

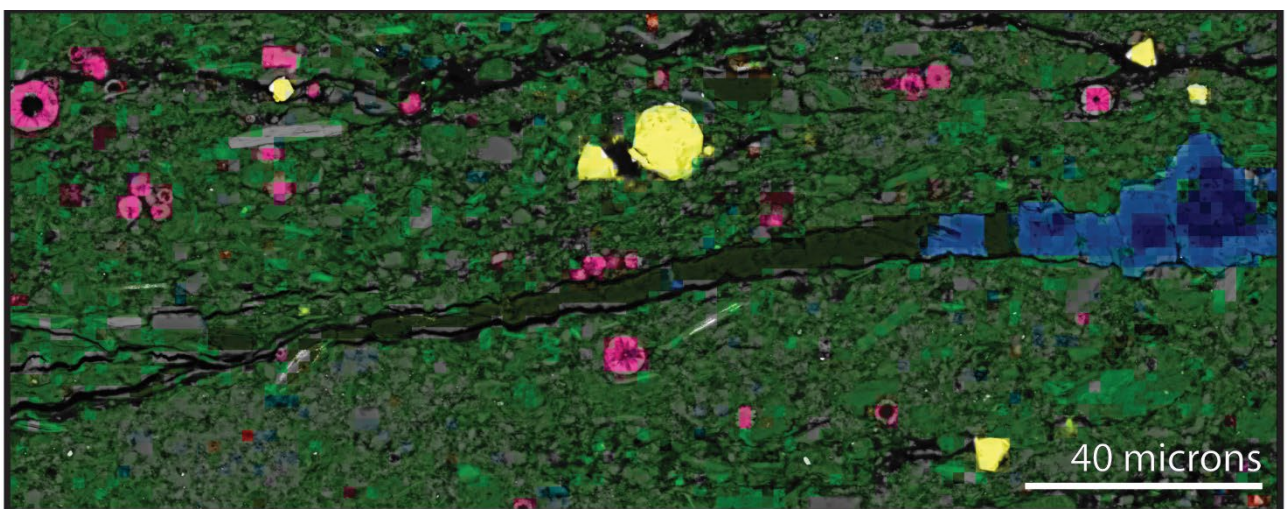


Figure 12: Fracture filled by dolomite – ankerite and later stage kaolinite or dickite.

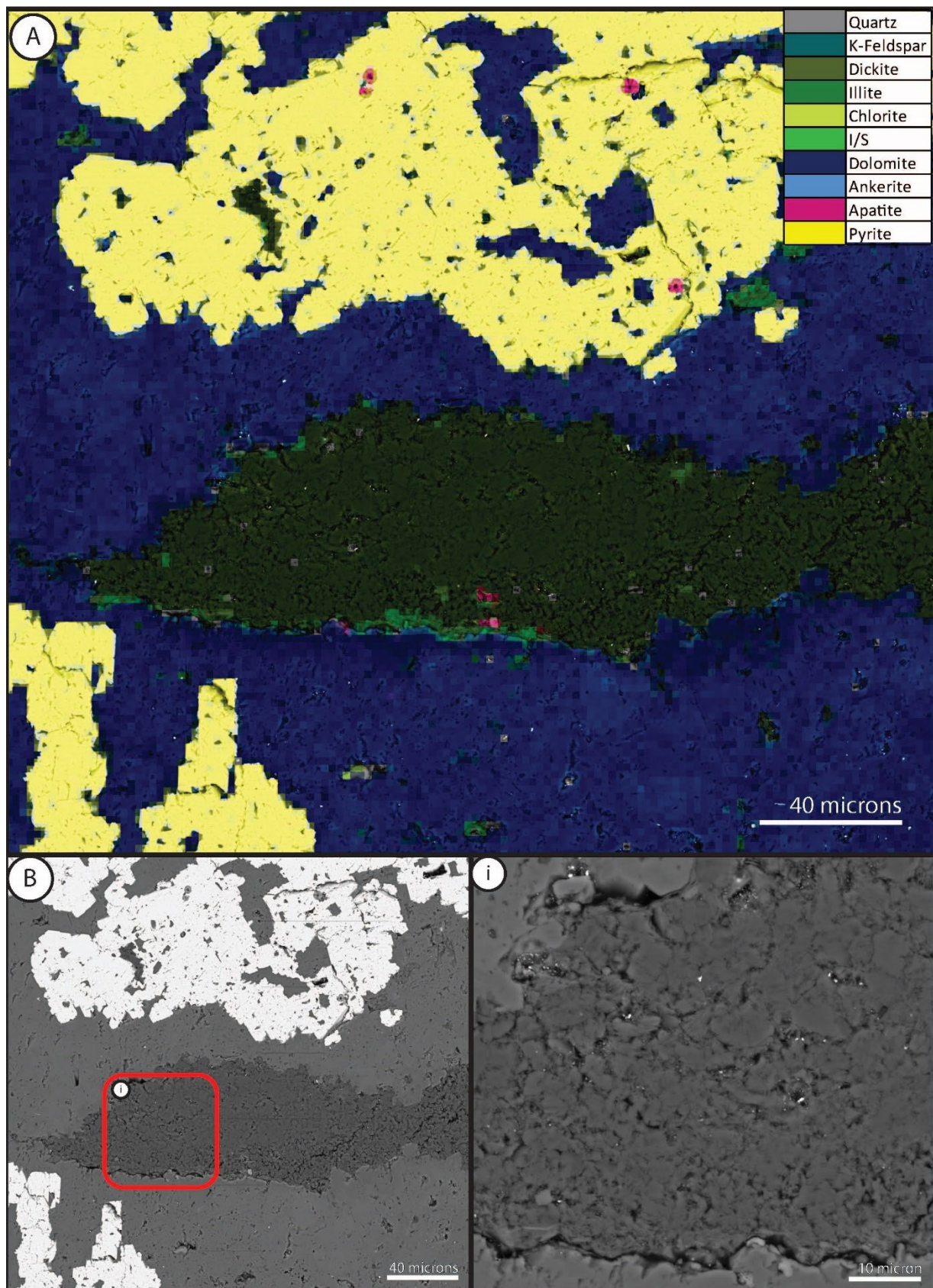


Figure 13: Euhedral diagenetic pyrite and late stage dickite mineralization within dolomite vein (161.25m). B(i) BSE image of dickite filling fracture within vein. Dickite occurs in ~ 5 micron 'books' randomly oriented and tightly packed. Minor euhedral quartz < 5 microns sporadically distributed throughout dickite fill.

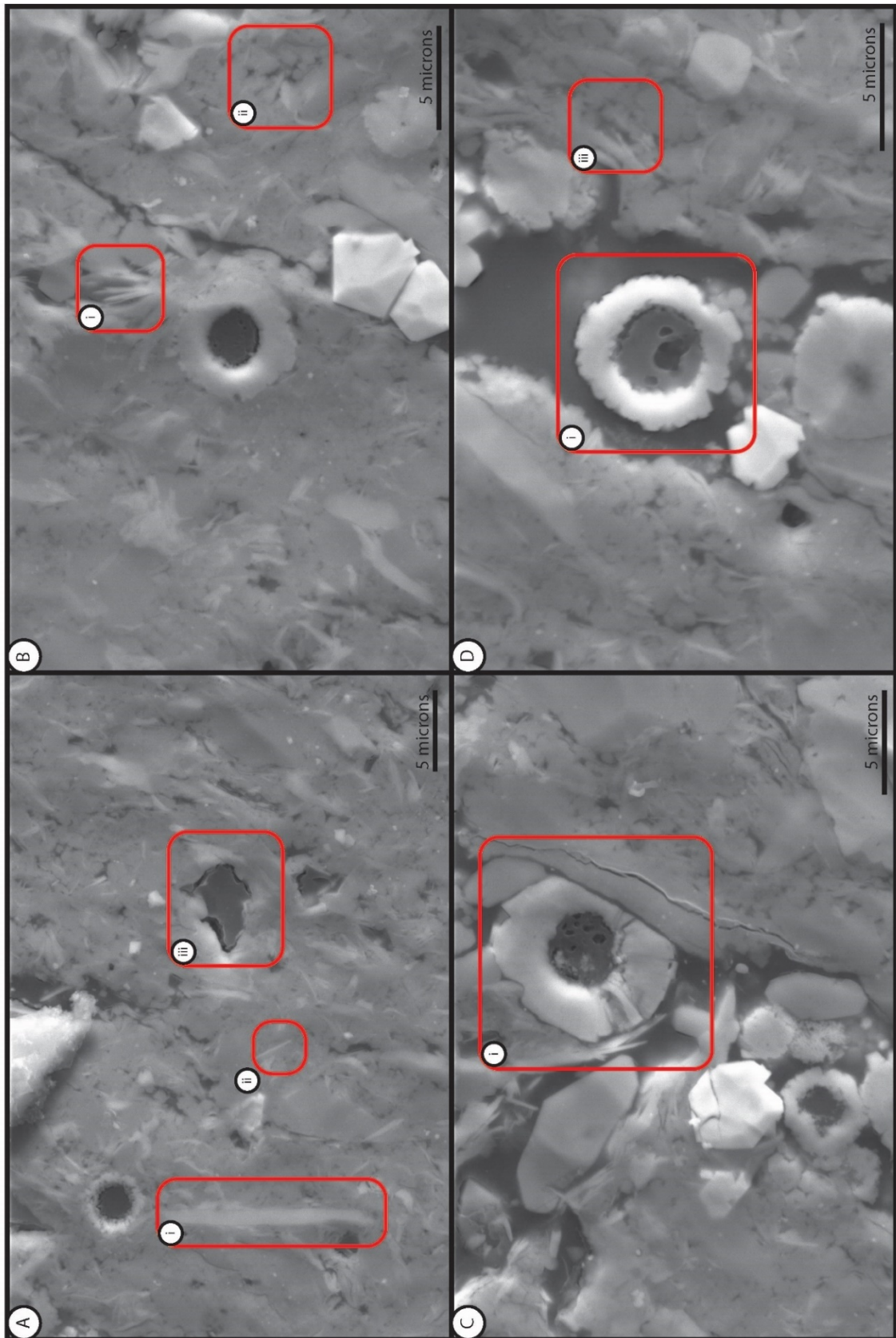


Figure 14: Secondary electron image of sedimentary matrix (114m). A(i) detrital mica ~ 5 microns. A(ii) diagenetic illite crystal. A(iii) porosity filling by organic matter. B(i) Diagenetic illite growth into porosity. B(ii) < 1-micron quartz crystals. Open space occurs between individual crystals. C(i) & D(i) apatite sphere grown in open porosity, and later filling by organic matter. D(ii) micro crystalline quartz matrix

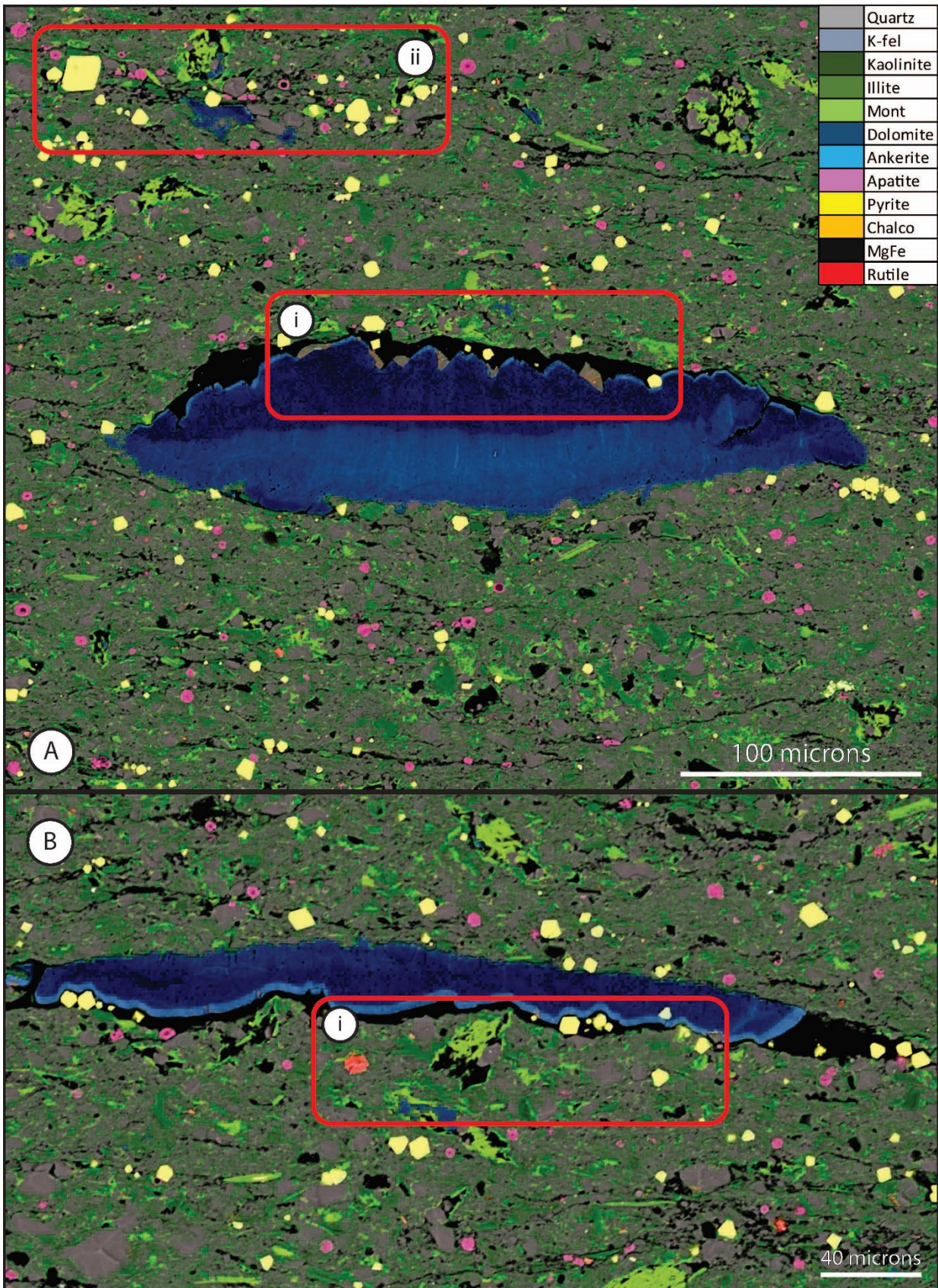


Figure 15: Fracture filling dolomite – ankerite. A(i): 217m Fe-Mg oxide precipitation on to rim of dolomite crystal and closely associated with ankerite rim. Interpreted to have syngenetically mineralized. A(ii): ~25-micron euhedral pyrite, hexagonal euhedral quartz, pore lining fibrous acicular chlorite and fracture filling dolomite identified as diagenetic phases. B(i) Ankerite rim on dolomite fracture fill contours to euhedral pyrite within fracture indicating paragenesis.

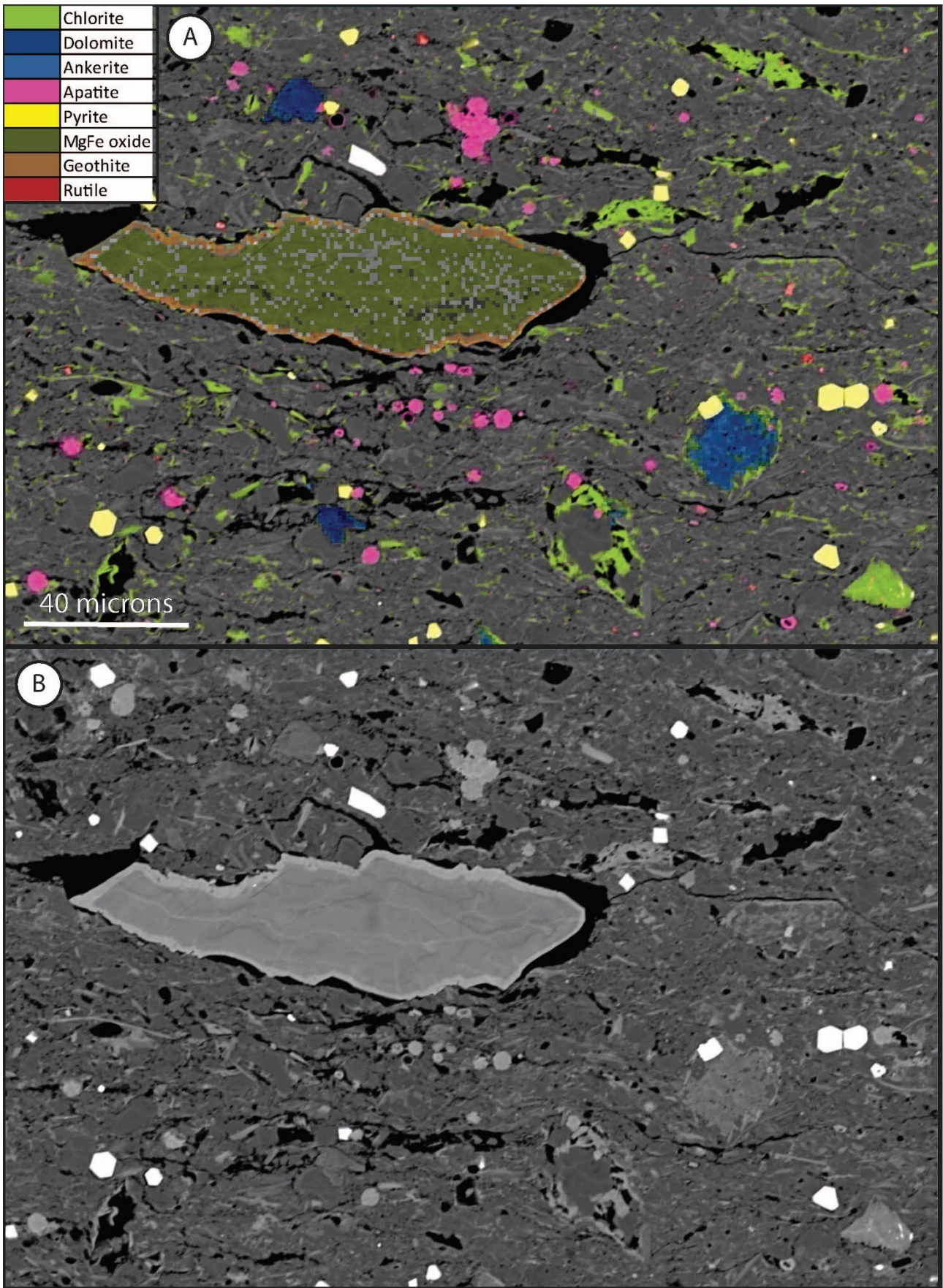


Figure 16: Diagenetic fracture filling iron oxides. Iron oxides show compositional zoning identified in BSE as density contrasts. EDX identifies greater intensity iron peaks on the rim (goethite) of oxide mineral, and a magnesium and iron peak across the core (magnesioferrite).

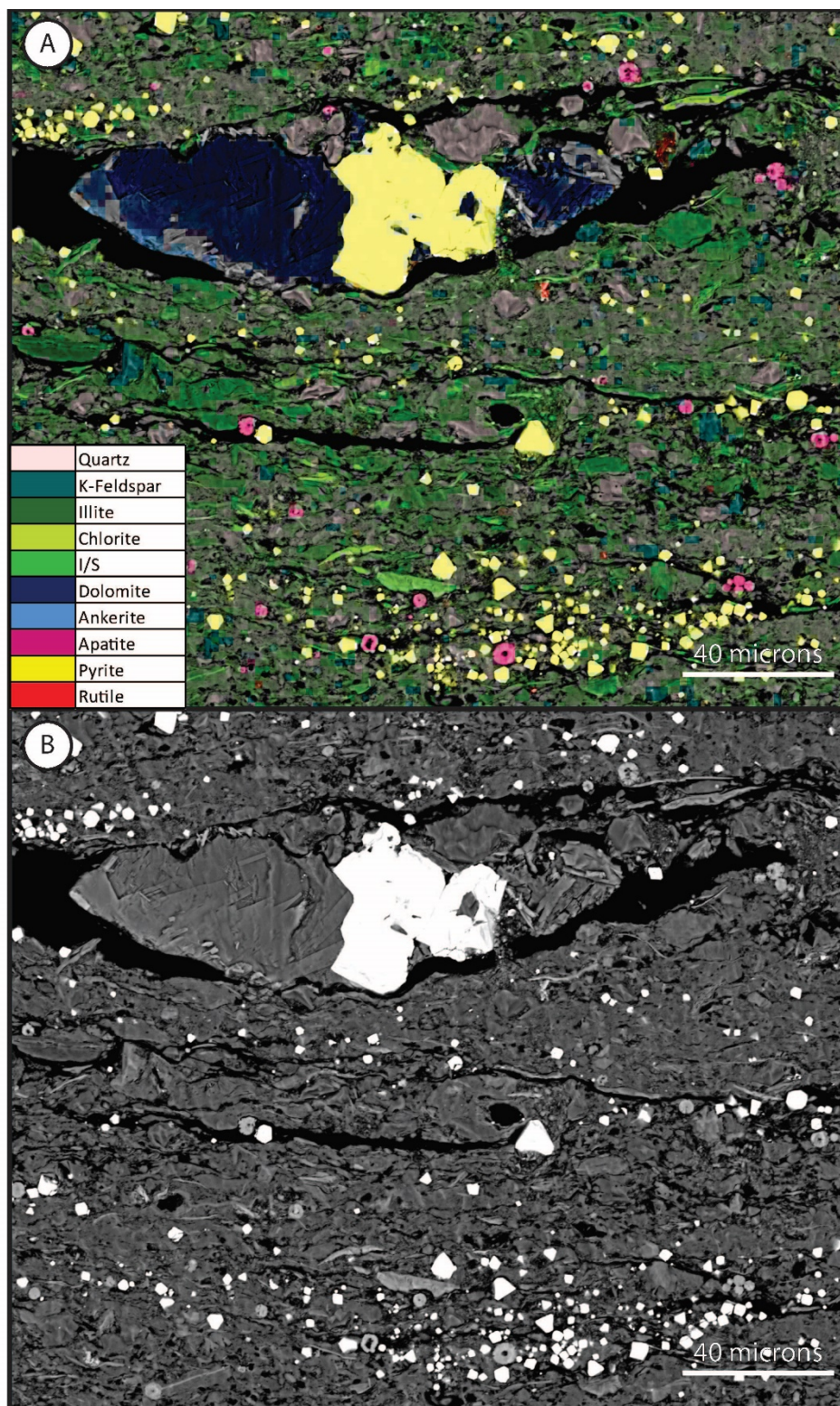


Figure 17: Diagenetic dolomite – ankerite and euhedral pyrite filling fracture in sedimentary matrix. ~ 20 micron diagenetic quartz situated above dolomite, within fracture.

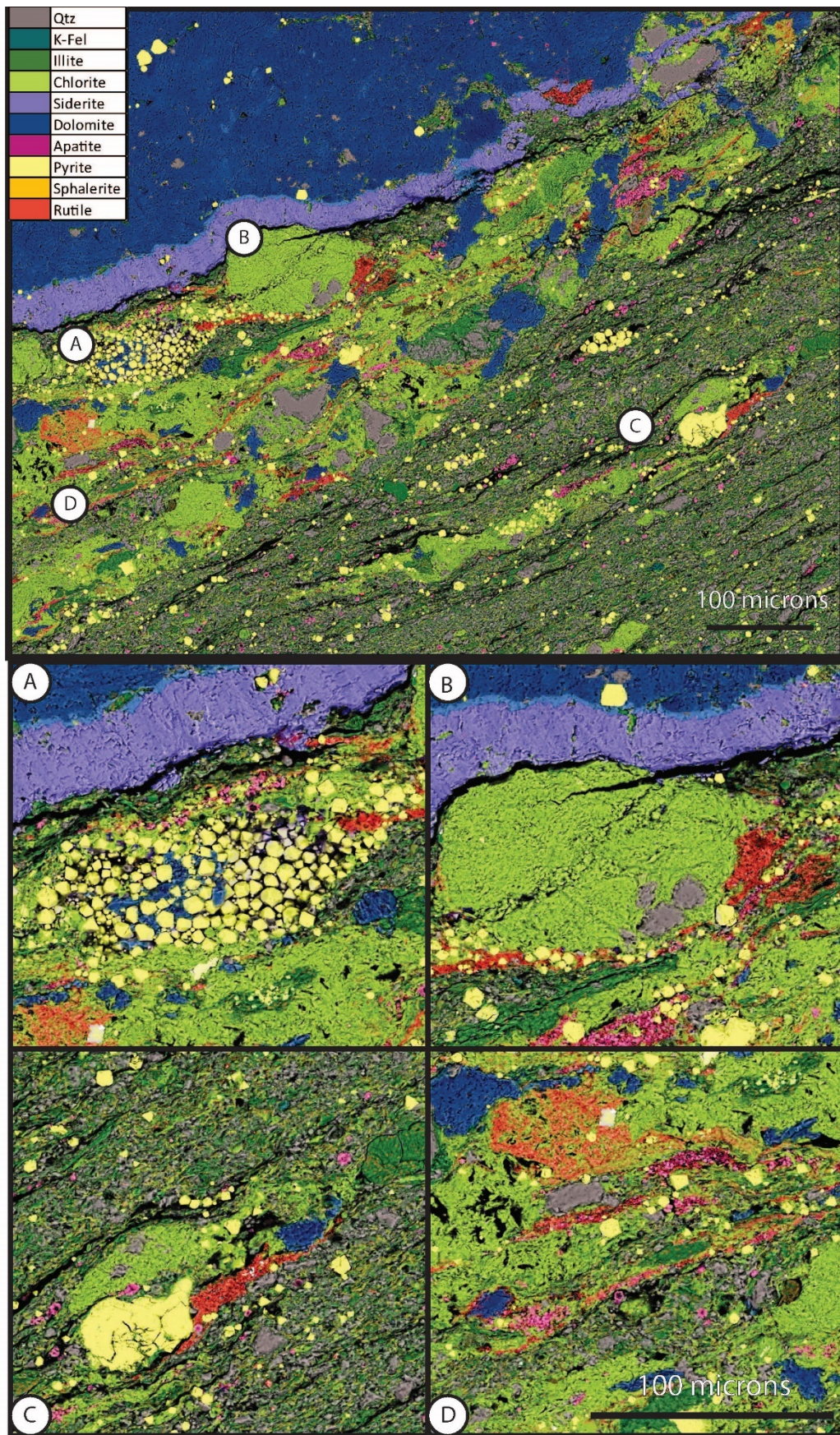


Figure 18: Sample 210.65m. Top panel shows dolomite – siderite vein as part of larger breccia cutting across shale matrix and heavily chloritized cavity fill. Chloritized filled are composed of diagenetic sulphides, titanium oxides and apatite micro-crystals.

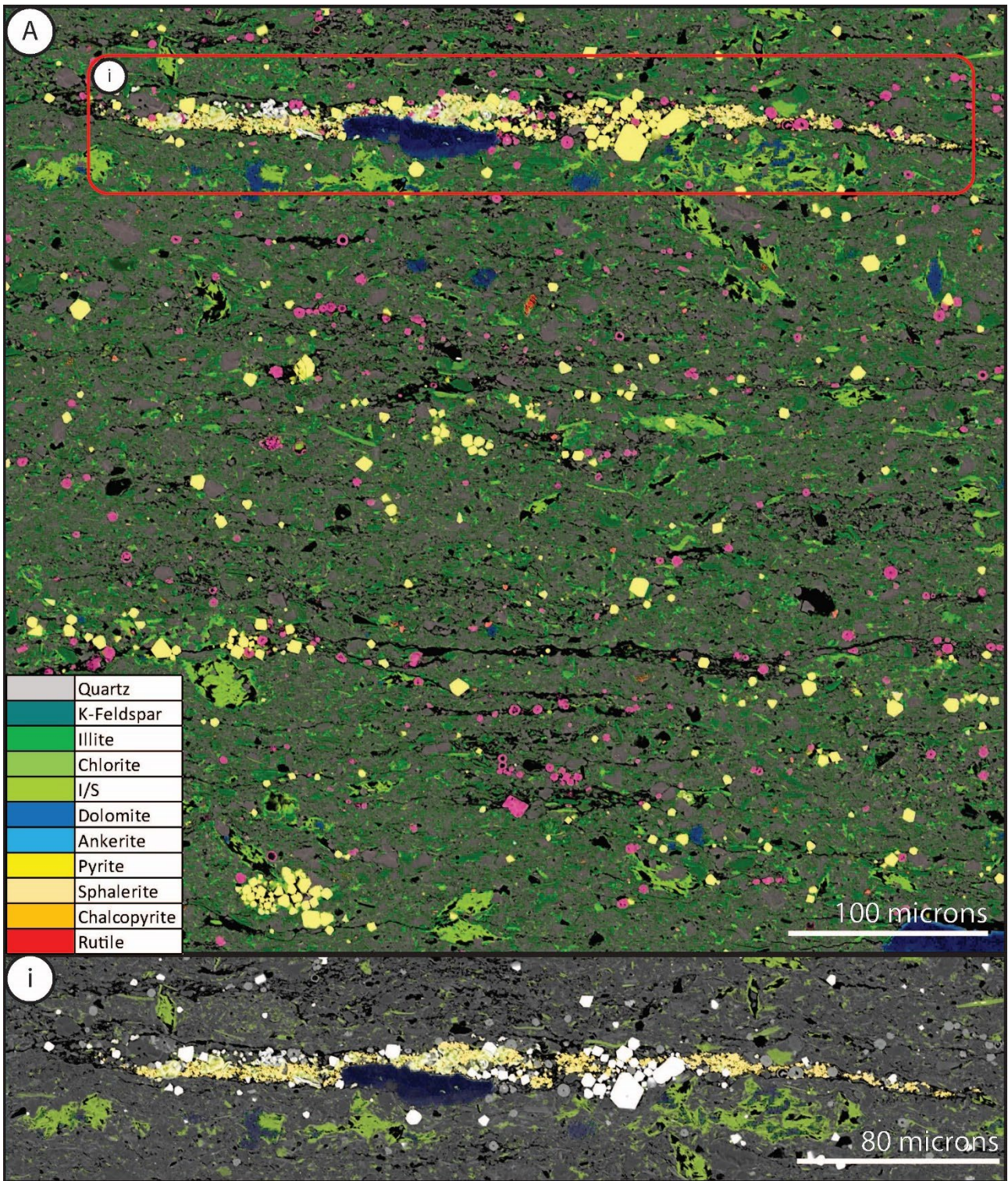


Figure 19: Fracture filled by pyrite, chalcopyrite, sphalerite and dolomite at 136m. Minor apatite and diagenetic quartz. Matrix composed of < 5-micron illite and quartz micro-crystals. Chlorite fills porosity as < 5 micron fibrous and acicular crystal intergrowths. Lower panel (i): Highlighted in yellow (sphalerite) and orange (chalcopyrite) to distinguish from pyrite (white). Dolomite crystal boundary suggests sulphides precipitated in two phases; initial euhedral pyrites, followed by Zn-Cu rich sphalerite and copper.

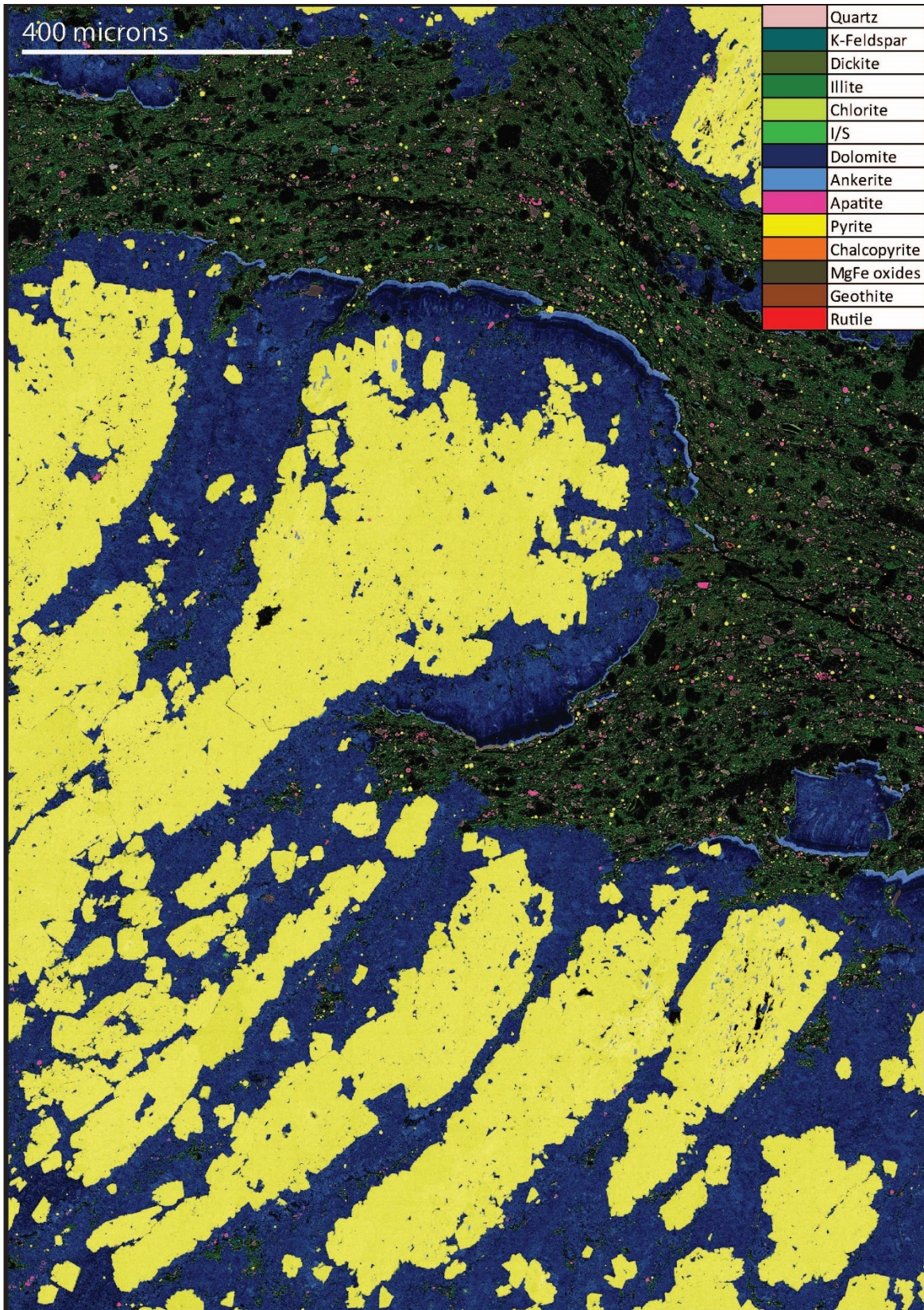


Figure 20: Heavily mineralized core segment at 151.58m. Pyrite occurs as 'stripes' within Dolomite – ankerite. Striped pattern indicates pyrite mineralization was confined to stratigraphic layering within diagenetic dolomite.

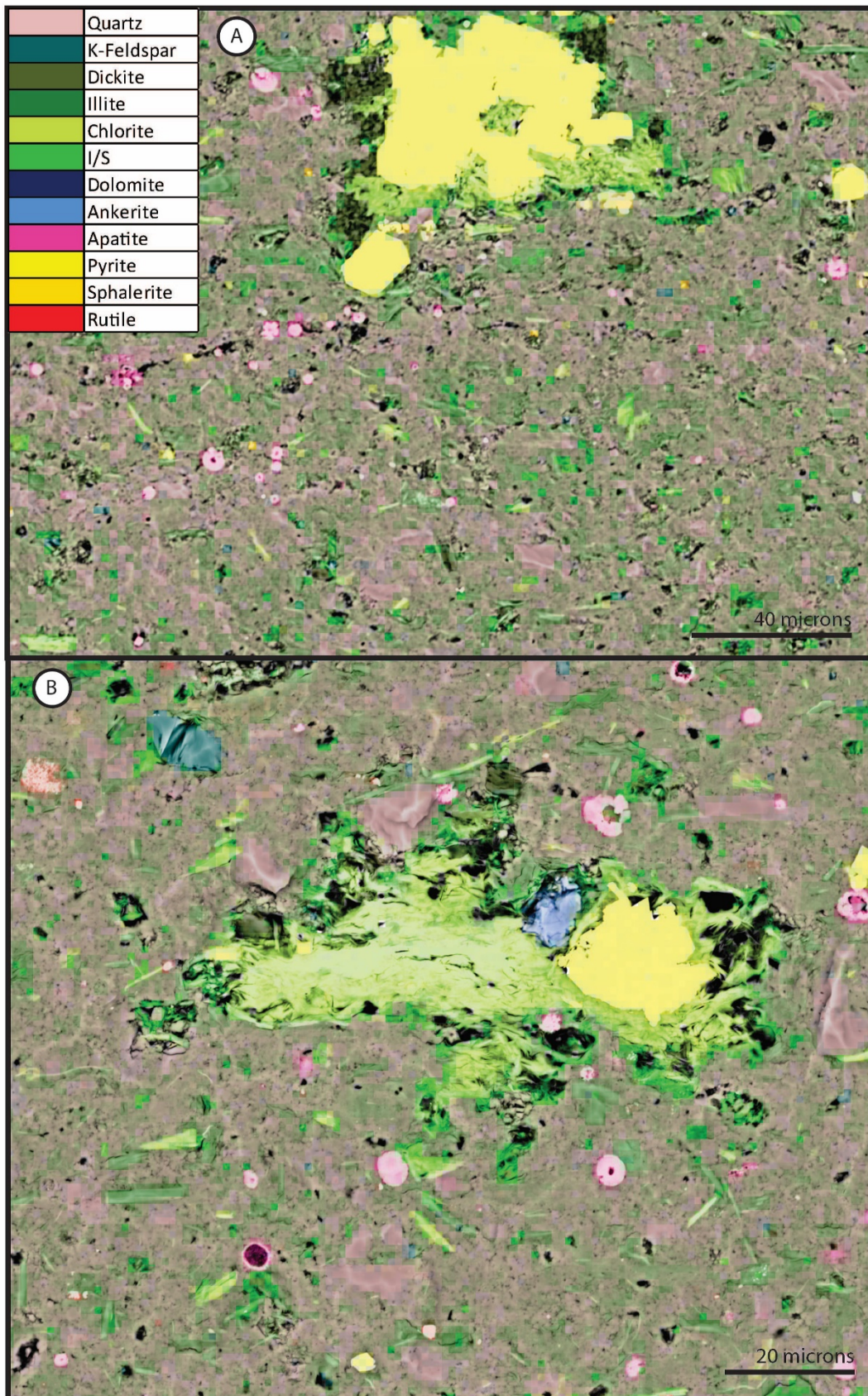


Figure 21: Pore filled by diagenetic chlorite, euhedral pyrite, dolomite and dickite. Pyrite, dolomite and late stage dickite are associated with vein mineralization. Sample at Depth 114m. Matrix is composed primarily of quartz and illite.

4. Discussion

The sediments of the Velkerri Formation potentially provide a rare insight into the paleoenvironmental conditions of the Mesoproterozoic because they have seen comparatively little deformation, burial and thermal heating. Most of the cores drilled through the Velkerri Formation show that it is just entering the oil window and in conjunction with its generally low porosity support the idea that diagenetic alteration of its original depositional redox chemistry was minor and occurred within a closed geochemical system conditions (Warren *et al.*, 1998; Shen *et al.*, 2002; Kendall *et al.*, 2009). The lithology of the Velkerri Formation is fine-grained and parallel laminated with little indication of remobilization of sediment by mass flow or currents. It thus provides a consistent temporal hemi-pelagic to pelagic record. The Urapunga-4 well was drilled as a stratigraphic research well and has been studied extensively as a paleo-environmental record of the Mesoproterozoic ocean (Jackson *et al.*, 1991; J. E. Gillott *et al.*, 2002; Kendall *et al.*, 2009). Re/Os dating provides broad temporal control placing the Formation around 1.4Ga (Kendall *et al.*, 2009). This correlates well with Rb-Sr ages on diagenetic Illite in the McMinn Formation, which date the Formation to 1429 ± 31 Ma (Kralik, 1982), and SHRIMP U-Pb zircon date of 1492 ± 31 Ma from a tuff layer within the Mainoru Formation (Abbott *et al.*, 2001). A minimum age for deposition of 1324 ± 4 of Roper Group sediments is recorded by SHRIMP U-Pb on baddeleyite in the intrusive Derim Derim Dolerite (Abbott *et al.*, 2001), and also provides a maximum age for deformation.

These factors have made Urapunga-4 the key reference section for the Mesoproterozoic and is considered one of the most reliable sources of paleo-redox information (Shen *et al.*, 2003; Arnold *et al.*, 2004). The sub-micron grain size of the Velkerri, however, has made conventional petrographic studies challenging because of the inability to resolve individual grains with conventional light microscopy and thus the majority of studies have employed bulk geochemical methods. The results here using FE-SEM to image at submicron scales show evidence of pervasive diagenetic and hydrothermal mineralization previously not recognized in the Urapunga-4 core.

Cross-cutting mineralized veins, and hydraulically brecciated intervals within the Urapunga-4 core indicate that the Velkerri Formation has been affected by post depositional high-temperature fluids. The sharp walls of the veins (Figure 2), cross cutting sedimentary laminae (Figure: 4), and mineralized brecciation (Figure 2) is evidence for brittle failure of cemented sediments with low porosity that encountered over pressured fluids. Interbedded intervals that are not cemented have euhedral pyrite, chalcopyrite and sphalerite present within micron scale pores suggesting diffusive

movement of fluids through intervals with greater permeability (Figure 3). Fractures created by overpressure acted as conduits for fluids and were progressively occluded and closed by a series of minerals that precipitated along the walls of the fractures (see below). 80 occurrences of veins were counted during logging of the Urapunga-4 core. They were most evident (78 of 80) in the highly cemented interval coinciding with the TOC peak in the Middle Velkerri Formation (118 – 225m). Mineralization within pores at microscopic scales that was not evident during logging was subsequently found in samples through the core suggesting pervasive fluid interaction through the Velkerri Formation. Veins in the Upper Member exhibit four distinct morphologies within the core; (i) centimeter-scale layered sparry dolomite veins with pyritic cores subparallel to bedding, (ii) fine (< 5mm) to very fine (< 1mm) cross cutting, white sinusoidal veins, (iii) cross-cutting mosaic breccias (Jebrak, 1997), and (iv) heavily pyritized intervals ~ 10 cm in core width (image). Mosaic breccias show cross cutting mineralized veins indicating multiple generations of mineralization, cementation, fracture, and fluid flow (image). In the Lower Velkerri Formation, a second TOC peak (324m – 326m: Figure 1) records abundant pyrobitumen filling splayed fractures, intra-particle (shelter) porosity and inter-particle porosity (discussed below). Pyrobitumen hosts authigenic pyrite, apatite, and sphalerite in a 2m thick migration fairway; 324-326m identifying a later fluid/diagenetic event resulting from hydrocarbon migration (326m) coinciding with samples that fall on the isochron of Kendall et al., (2009).

Veins are filled with dolomite, ankerite, pyrite, chalcopyrite, sphalerite, rutile, dickite, chlorite, apatite, quartz and iron oxides determined using Nanomin mapping. These same minerals also occur in pores within the sedimentary matrix at the micron scale. Dolomite and pyrite comprise > 90% of the diagenetic mineral phases filling the veins. Later stage ankerite filling veinlets cut across dolomite veins. Ankerite filled veinlets also host authigenic iron oxides and fragments of brecciated euhedral pyrite. Pyrite fragments have sharp jigsaw like pieces with ankerite fill between them, they and do not show evidence of dissolution, but appear to result from breakage within the veins and must have formed occlusions to fluid flow. Dolomite most often forms the first vein lining mineral and subsequently hosts pyrite, chalcopyrite in the centre of veins. Kaolinite and Dickite also occurs in the centre of some veins but is isolated in clusters of pure dickite (>99% of mineral by area). Veins are thus systematically layered with ankerite, dolomite, pyrite, chalcopyrite, and later stage alteration to chlorite (210.65m), as well as late stage dickite precipitation within dolomite fractures (Figure 7, 12, 13). Chlorite is distributed as a crystalline cement within fractures and pores and is typically acicular and fibrous (Figure 14, 18, 19, 21). Iron – magnesium oxides are associated with

late stage cross cutting ankerite fluids in breccia. Iron oxides occur filling fractures in a similar morphology to diagenetic dolomite (Figure 16) or occur on the periphery of diagenetic dolomite crystals (Figure 15 A, *i.*). Preceding the carbonate phases are chloritized breccia cavity fills containing diagenetic pyrite, rutile and apatite. Later stage dolomite filled the open porosity within these breccias. Quartz cements occurred in at least two distinct events. The common cement is comprised of approximately < 1 micron in diameter and are intergrown with < 1-micron Illite crystals (Figure 14: A, *i*, B, *i*, *ii*). This is a pore filling cement and comprises up to 50% of the rock indicating an early (pre-compaction) origin. Micro crystals can grow together forming aggregates up to 10 microns in diameter that may give the appearance of detrital quartz silt. Quartz also can form overgrowths on detrital quartz grains (Figure 18: B, D). Diagenetic dolomite and pyrite cross cut quartz – Illite cements and occurred post cementation (Figure 7, 8, 17) based on evidence of brittle fracture. A second generation of diagenetic quartz also occurs within dolomite veins and sedimentary fractures. This more crystalline quartz occurs in fractures as either; (i) euhedral crystals (Figure 10: B), or (ii) recrystallized aggregates filling porosity in carbonates and chloritized intervals. Hexagonal crystalline quartz occurs within dolomite porosity (Figure 10: A) and in fractures within the sedimentary matrix (Figure 10: B).

Late stage fluid movement and mineralization in the Velkerri Formation has been recognized in the context of mineral and hydrocarbon investigation within the McArthur Basin in general, however the Urapunga-4 core has been considered by many researchers as unaffected (Shen *et al.*, 2002; Kendall *et al.*, 2009). $\delta^{34}\text{S}$ has been used in combination with DOP and $\text{Fe}_{\text{HR}}/\text{Fe}_{\text{Total}}$ to support the hypothesis of a stratified ocean with the assumption that all pyrite (Fe) is sourced from water column sources (Shen *et al.*, 2002). Live oil is documented (Jackson *et al.*, 1986) in the Urapunga-4 core at a depth of 345.4m to 346.5m indicating hydrocarbon migration requiring an open system for fluids. In this study, BSEM imaging revealed evidence for fractures cutting across sedimentary bedding and filled with pyrobitumen, particularly in the lower TOC peak from 324 – 326m. These fractures commonly have accumulations of >20-micron euhedral pyrite crystals lined within their cores. Shelter porosity within apatite spheres is filled by bitumen as is intragranular porosity at micron and submicron scales (Figure 10). Silica cement comprised of micro-scale quartz common in the upper TOC peak of the Velkerri Formation is not present in this lower peak and porosity is greater as a result. Thucolites, which are 40 micron balls of pyrobitumen with radioactive mineral core (Revie, 2017) are present in the Urapunga-4 core and record radiation damage and retention

of a small fraction of a large volume of migrating hydrocarbons, again pointing to open fluid pathways.

The variety, morphology and distribution of diagenetic minerals within a series of cross cutting veins and breccias (including fragmented diagenetic minerals) indicates that multiple fluid events flowed through fractures and were varied in composition through time. This likely reflects a fluid flow pathway driven by a prolonged thermal source with changes in fluid plumbing as fractures were filled by minerals and overpressure opened new pathways sometimes re-opening past mineralized areas. Chloritized 10 to 50-micron scale breccias containing authigenic rutile, apatite, sphalerite and pyrite fill cavity linings between diagenetic carbonates (Figure 18: B, D), and diagenetically cemented sediments (Figure 18: C). Diagenetic quartz is also evident within chloritized breccias (Figure 18: C). Diagenetic dolomite – ankerite and pyrite cut across chloritized breccias (Figure 18: A, C, D), and fill porosity within fractures affected by diagenetic chlorite precipitation (Figure 16: A, & figure 19). Iron oxides are associated with ankerite veins which cut across previous dolomite veins (Figure 8: *i*). Diagenetic sulfides; pyrite, chalcopyrite, and sphalerite may potentially have occurred during or after dolomite mineralization. Sulfides predominantly occur in the centre of dolomite – ankerite veins, but not within cross cutting ankerite veins, and occur within chloritized breccias. Pyrite also occurs in porosity and fractures within the sedimentary matrix. These pyrites are euhedral and occur in clusters or as isolated crystals. Pyrite crystals within aggregates have a dodecahedral geometry and vary in size from 5 – 20 microns (Figure 18: A). Aggregates can also contain micro crystalline (< 2micron) chalcopyrite and sphalerite (Figure 19: *i*). Sulfides however do not occur with dickite/kaolinite, which occurs in two morphologies; as (1) replacement of detrital grains in the cemented sedimentary matrix (Figure 11), and (2) in porosity within diagenetic dolomite – ankerite veins (Figure 7, 13). Replacement by dickite in sediments may have occurred prior to the intrusion of hydrothermal fluids, however dickite kaolinite filling porosity indicates late stage movement of silicate rich fluids through fractured intervals. The distribution of dickite and the lack of sulfides also indicates that sulfide precipitation occurred prior to the precipitation.

The temperature of the diagenetic fluids is constrained by; a) mineral assembly, b) $\delta^{18}\text{O}$ values and clumped isotope values of carbonates. Dickite, chalcopyrite, and sphalerite are

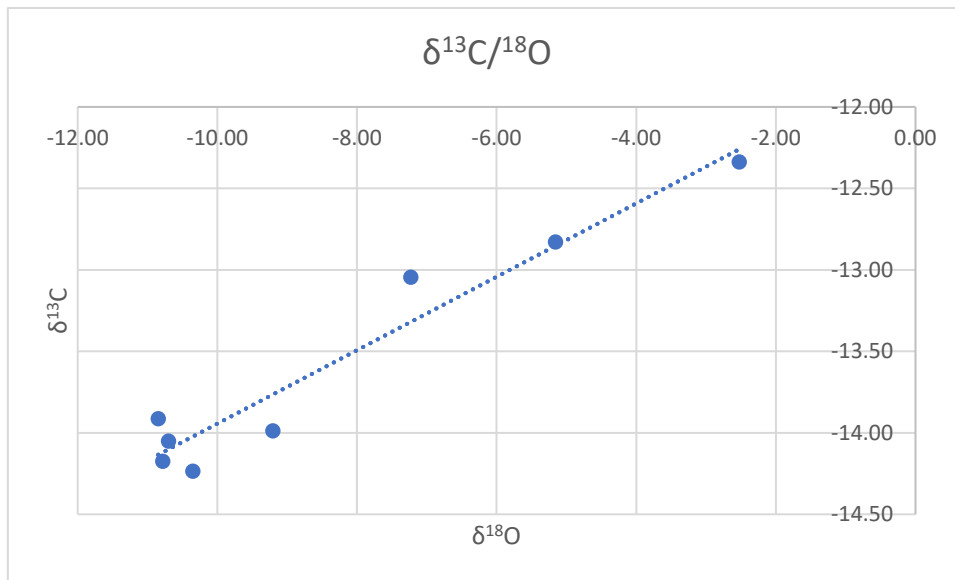


Figure 22: $\delta^{13}\text{C}/\delta^{18}\text{O}$ values indicating more than one fluid composition. R^2 value of linear regression = $R^2 = 0.9369$.

indicative of higher fluid temperatures typical of hydrothermal systems (Rye *et al.*, 1981; Parnell *et al.*, 2004). Clumped Isotope thermometry was conducted on 10 carbonate samples from veins and breccias for the purpose of estimating the temperature of hydrothermal fluids. Carbonate clumped isotope thermometry is a paleotemperature proxy based on measurements of the degree of ordering of ^{13}C and ^{18}O into bonds with each other (constituting the $^{13}\text{C}^{18}\text{O}^{16}\text{O}_{2-2}$ ion group) (Dennis, 2011; Eiler, 2011). Clumped isotope thermometry constrains the temperature of fluids independent of the isotopic composition of the precipitating fluids (Defliese, Hren, & Lohmann, 2015; Murray, Arienzo, & Swart, 2016; Staudigel *et al.*, 2018). The $\delta^{13}\text{C}/\delta^{18}\text{O}$ ratio from carbonate samples indicate isotopic contribution of oxygen from more than one fluid based on the linear trend presented in (Figure 22) with both end members too depleted to be of a primary marine (depositional) origin.

Measured $\delta^{18}\text{O}$ ranged from -9.6% to -14.2% , with all but one sample falling in the range -12.3 to -14.2% (Table 1). These values are consistent with heated groundwaters. Clumped isotope palaeothermometry based on $\Delta 47$ measurements estimate a range of precipitation temperatures from $88\text{ }^\circ\text{C}$ to $201\text{ }^\circ\text{C}$ (Table 1). These temperatures are greater than that of expected burial temperatures ($\sim 75\text{ }^\circ\text{C}$ – $150\text{ }^\circ\text{C}$) (Cook *et al.*, 1988; Summons *et al.*, 1994; Warren *et al.*, 1998; George *et al.*, 2002; Ahmad *et al.*, 2013; Flannery *et al.*, 2014).

A potential source of heat and fluids within the Velkerri Formation may be the intrusive Derim Derim dolerite suite (Abbott *et al.*, 2001). The Derim Derim dolerite has an intrusion age of 1324 ± 4 ma measured on baddeleyite U-Pb (SHRIMP) (Abbott *et al.*, 2001). While the Derim Derim dolerite was not intersected in the Urapunga-4 core, it is present in the Urapunga-5 core $< 10\text{km}$ away where it

intrudes into the Bessie Creek and Moroak Sandstone. The Derim Derim Dolerite is widespread, intruding as sills and dykes within the Urapunga Fault zone (Abbott *et al.*, 2001). It has been suggested to have affected the Velkerri Formation in other locations based on thermally altered and matured organic matter (T. H. Donnelly *et al.*, 1988; Summons *et al.*, 1994; George *et al.*, 2002). Fluid temperatures estimated using clumped isotope palaeothermometry (88 °C – 201 °C) are comparable to fluid temperatures that emplaced the HYC deposit in the MacArthur River region (~260 °C) (Rye *et al.*, 1981), and within the expected range for maturation of hydrocarbons by igneous intrusion (75 - 150 °C) (T. H. Donnelly *et al.*, 1988; Summons *et al.*, 1994; George *et al.*, 2002). The Urapunga fault zone offers a potential conduit for fluid flow throughout the Roper Group sediments, which affect The Urapunga cores (1-6). Carbonate hosted Zn – Pb Mineralization is identified within the Mt Vizard group approximately 20 km east of the Urapunga 4 core associated with intrusion by the Derim Derim dolerite (Abbott *et al.*, 2001). Mineralization is composed of disseminated galena, chalcopyrite, and sphalerite in brecciated and silicified dolomite veinlets (Crabb, 1995; Abbott *et al.*, 2001) not too dissimilar to those described here. Dolomite filling veins might be sourced from dissolution of carbonates present within units such as the Balbirini Dolomite (Abbott *et al.*, 2001).

Similarly, the Wollogorang Formation as part of the Tawallah group has been suggested to be affected by post – depositional hydrothermal fluid migration caused by intruding igneous bodies (Kendall *et al.*, 2009). Scatter about the Re-Os isochron in the Wollogorang fm. has been suggested as an indication of hydrothermal fluid alteration (Kendall *et al.*, 2009). Previous work by Donnelly & Jackson *et al.*, (1988) also noticed cross cutting carbonate veinlets which are interpreted as dolomitic breccias. Fluids are associated with igneous activity during the Mt Isa Superbasin Phase, which is responsible for the emplacement of the Carpentaria Line Zinc deposits (Kendall *et al.*, 2009). This is supported by Cooke *et al.*, (1998), who suggested the Regional Settlement Creek and Gold Creek Volcanics as the potential sources of low temperature (~ 100 °C) oxidizing and saline (>20 wt% NaCl equivalent) during igneous sill intrusion (Cooke *et al.*, 1998). Brines are also thought to be responsible for the leaching of base metals which migrated through the Wollogorang fm. (Cooke *et al.*, 1998; Garven *et al.*, 2001; Kendall *et al.*, 2009). Hydrothermal fluids have been identified within the McArthur basin in multiple locations and are associated with regional tectonic extension (Abbott *et al.*, 2001). Most notably is the McArthur River “HYC” sediment hosted lead-zinc-silver deposit within the Barney Creek fm., as emplacement by hot basinal brines circulated through faults has been hypothesized (Williams, 1978; Rye *et al.*, 1981; Perkins, 1984; Jackson *et al.*, 1987; Chen *et al.*,

2003) as well as syn-sedimentary deposition (Garven *et al.*, 2001). Williams (1978) identified two generations of pyrites within HYC pyritic shales and observed diagenetic alteration of framboidal pyrite to euhedral pyrite as a result of mineralizing fluids. It has been suggested that variations of maturity within the Barney Creek fm. hydrocarbons have been affected by changes in geothermal gradients as a result of infiltrating hydrothermal fluids (Powell *et al.*, 1987). The McArthur river deposit shows greater mineralization than in any other location in the McArthur basin, however an analogy of formation can be drawn between the HYC deposit, the mineralized Mt Vizard prospect, and the Urapunga – 4 Core. Mineralized units lie adjacent to major regional faults and are intruded by igneous bodies along faults. Igneous intrusion is a local sources of heat and drives circulation of fluids through faults and sediments (Rye *et al.*, 1981; Powell *et al.*, 1987; Eldridge *et al.*, 1993; Abbott *et al.*, 2000, 2001; Chen *et al.*, 2003).

Introduction of hydrothermally derived pyrite, iron oxides, rutile, and other iron – sulfide minerals from high temperature fluids likely affected the total iron budget and other redox sensitive elements of the Velkerri Formation used as paleoredox indicators in Urapunga - 4. Introduction of diagenetic pyrite from fluids sourced out of the immediate sedimentary beds adds additional Fe and S to the DOP of sediments, changing the ratio Fe_{HR}/Fe_T , Fe – S – C systematics (Canfield *et al.*, 1986; Raiswell *et al.*, 1988; Jenkyns *et al.*, 2006). The sulfur contribution evident in pyrite and sphalerite would also influence the sulfur isotope composition of bulk pyrite in Urapunga – 4 which shows a 40‰ shift in $^{32}S/^{34}S$ (Shen *et al.*, 2002) that has been attributed to increased sulfate reduction from initial oxygenation of the ocean (Shen *et al.*, 2003) but also coincides with the interval corresponding with the greatest evidence for hydrothermal alteration documented here. ^{34}S shows the same range of variability in the Newland Formation (~40‰) in which a combination of sulfate reduction within sediments and hydrothermal Fe + S are recognized (Strauss *et al.*, 1990; Shen *et al.*, 2003). Similarly in recent Red Sea sedimentary geothermal deposits, sulfur isotope values indicate a ~40‰ range in $^{32}/^{34}S$ attributed to combined bacterial sulfate reduction from seawater and the introduction of hydrothermally derived sulfur (Shanks *et al.*, 1980). The contribution of a diagenetic source of iron oxides similarly affects the index of reactive iron attributed only to iron oxide sourced from seawater (Shen *et al.*, 2003). Re-Os systematics may also have been affected as Re and Os are both siderophiles (Shirey *et al.*, 1995; Stein, 1997; Stein *et al.*, 1998; Hannah *et al.*, 2004) and associated with organic carbon (Ravizza *et al.*, 1989, 1993; Cohen, 2004) and both S and organic carbon show alteration in the Urapunga-4 intervals used to establish the age of the formation using the Re/Os geochronometer assuming only a seawater source of these elements. In the McArthur Basin, Re-Os

geochronology has been applied to the Velkerri and Wollogorang Formations. Isochrons constrain two depositional ages for the Velkerri Formation: 1361 ± 21 Ma, and 1417 ± 29 Ma, and one for the Wollogorang Formation at 1359 ± 150 Ma. The greater variability in the Wollogorang Formation has been attributed to hydrothermal fluids (Kendall *et al.*, 2009).

The relative abundance of pyrite from diagenetic sources can be estimated using the Nanomin system. The Nanomin system can determine the abundance of minerals by correlating x-ray spectra and mineral textures (see methods). From this the mineral composition of samples can be calculated as an area percentage. Pyrite forming in modern euxinic and anoxic depositional environments exhibit framboidal and euhedral morphologies (Wilkin *et al.*, 1996, 1997). However diagenetic pyrite as described above, has a distinct cross cutting and late stage relationship with sediments and constitutes > 90% of pyrite in some samples (Figure 5, 8, 13 20). The calculated area percentage of pyrite within samples ranges from 2% – 50% of the total area (Table 2: supplementary data). It is difficult to constrain the overall abundance of diagenetic pyrite, but it is estimated to comprise > 20% of total pyrite in the Velkerri Formation.

5. Conclusions

The presence of cross cutting veins infilled by iron-magnesium carbonate minerals, significant diagenetic pyrite, iron oxides, and base metal sulfides and hydrocarbon migration indicate that the Velkerri Formation is affected by hydrothermal fluids and hydrocarbon migration that contribute to a complex multi-phase diagenetic history. The presence of these minerals in veins as well as diffusive fronts in pores suggests that much of the Velkerri Formation in the Urapunga-4 core has undergone significant modification of Fe budgets at micro scale even where veins are not immediately apparent from visual inspection. The variable composition of hydrothermal minerals suggests fluid composition evolved over time. Sediments are composed of up to 60% diagenetic quartz – Illite, with microporosity that has been filled later by diagenetic carbonate, sulfide, and oxide minerals. This strong diagenetic influence was not just driven by local recrystallization in a closed system but reflects open system movement of fluids and thus would have significantly influenced the isotopic and mass fraction of elements used as paleo-redox proxies to calculate oxygen concentration of Mesoproterozoic seawater.

6. References

- Abbott, S. T. *et al.* (2001) *ROPER REGION : URAPUNGA and ROPER RIVER Special , Northern Territory (Second Edition)*.
- Abbott, S. T. and Sweet, I. P. (2000) 'Tectonic control on third-order sequences in a siliciclastic ramp-style basin: An example from the Roper Superbasin (Mesoproterozoic), northern Australia', *Australian Journal of Earth Sciences*, 47(3), pp. 637–657. doi: 10.1046/j.1440-0952.2000.00795.x.
- Ahmad, M. and Munson, T. (2013) *Geology and mineral resources of the Northern Territory*.
- Anbar, A. D. *et al.* (1992) 'Rhenium in seawater: Confirmation of generally conservative behavior', *Geochimica et Cosmochimica Acta*, 56(11), pp. 4099–4103. doi: 10.1016/0016-7037(92)90021-A.
- Anbar, A. D. *et al.* (2007) 'A Whiff of Oxygen Before the', *Science*, 317(September), pp. 1903–1907. doi: 10.1126/science.1140325.
- Arnold, G. L. *et al.* (2004) 'Molybdenum Isotope Evidence for Widespread Anoxia in Mid-Proterozoic Oceans', *Science*, 304(5667), pp. 87–90. doi: 10.1126/science.1091785.
- Balci, N. *et al.* (2007) 'Oxygen and sulfur isotope systematics of sulfate produced by bacterial and abiotic oxidation of pyrite', *Geochimica et Cosmochimica Acta*, 71(15), pp. 3796–3811. doi: 10.1016/j.gca.2007.04.017.
- Bekker, A. *et al.* (2004) 'Dating the rise of atmospheric oxygen', *Nature*, 427(6970), pp. 117–120. doi: 10.1038/nature02260.
- Bekker, A. *et al.* (2010) 'Iron formation: The sedimentary product of a complex interplay among mantle, tectonic, oceanic, and biospheric processes', *Economic Geology*, 105(3), pp. 467–508. doi: 10.2113/gsecongeo.105.3.467.
- Berner, R. A. (1984) 'Sedimentary pyrite formation: An update', *Geochimica et Cosmochimica Acta*, 48(4), pp. 605–615. doi: 10.1016/0016-7037(84)90089-9.
- Berner, R. A. and Raiswell, R. (1983) 'Burial of organic carbon and pyrite sulfur in sediments over phanerozoic time: a new theory', *Geochimica et Cosmochimica Acta*, 47(5), pp. 855–862. doi: 10.1016/0016-7037(83)90151-5.
- Canfield, D. E. *et al.* (1986) 'The use of chromium reduction in the analysis of reduced inorganic sulfur in sediments and shales', *Chemical Geology*, 54(1–2), pp. 149–155. doi: 10.1016/0009-2541(86)90078-1.
- Canfield, D. E. (1989) 'Reactive iron in marine sediments', *Geochimica et Cosmochimica Acta*, 53(3), pp. 619–632. doi: 10.1016/0016-7037(89)90005-7.
- Canfield, D. E. (1998) 'A new model for Proterozoic ocean chemistry', *Nature*, 396(6710), pp. 450–453. doi: 10.1038/24839.
- Canfield, D. E. (2005) 'THE EARLY HISTORY OF ATMOSPHERIC OXYGEN: Homage to Robert M. Garrels', *Annual Review of Earth and Planetary Sciences*, 33(1), pp. 1–36. doi: 10.1146/annurev.earth.33.092203.122711.
- Canfield, D. E. *et al.* (2008) 'Ferruginous Conditions Dominated Later Neoproterozoic Deep-Water Chemistry', (August), pp. 949–953. Available at: <http://www.sciencemag.org/content/315/5808/92.short>.
- Canfield, D. E., Habicht, K. S. and Thamdrup, B. (2007) 'The Archean Sulfur Cycle and the Early History of Atmospheric Oxygen', 658(2000), pp. 658–662. doi: 10.1126/science.288.5466.658.
- Canfield, D. E. and Teske, A. (1996) 'Late proterozoic rise in atmospheric oxygen concentration inferred from phylogenetic and sulphur-isotope studies', *Nature*, pp. 127–132. doi: 10.1038/382127a0.

- Canfield, Poulton, S. and Narbonne, G. (2007) 'Late-Neoproterozoic Oxygenation and the Rise of Animal Life', *Science*, 315(5808), pp. 92–95. Available at: <http://www.sciencemag.org/content/315/5808/92.short>.
- Chen, J. *et al.* (2003) 'The Paleoproterozoic McArthur River (HYC) Pb/Zn/Ag deposit of northern Australia: Organic geochemistry and ore genesis', *Earth and Planetary Science Letters*, 210(3–4), pp. 467–479. doi: 10.1016/S0012-821X(03)00171-7.
- Cloud, P. (1972) 'A working model of the primitive Earth', *American Journal of Science*, pp. 537–548. doi: 10.2475/ajs.272.6.537.
- Cohen, A. S. (2004) 'The rhenium-osmium isotope system: applications to geochronological and palaeoenvironmental problems', *Journal of the Geological Society*, 161(4), pp. 729–734. doi: 10.1144/0016-764903-084.
- Cook, I. H. C. J. B. A. C. and Powell, T. G. (1988) 'Petroleum Geology and Geochemistry of Middle Proterozoic McArthur Basin, Northern Australia II: Assessment of Source Rock Potential', 12(12), pp. 1495–1514.
- Cooke, D. R. *et al.* (1998) 'K-metasomatism and base metal depletion in volcanic rocks from the McArthur basin, northern territory-implications for base metal mineralization', *Economic Geology*, 93(8), pp. 1237–1263. doi: 10.2113/gsecongeo.93.8.1237.
- Crabb, D. M. (1995) *MIM Exploration PTY LTD Technical Report No. 2527*.
- Creaser, R. A. *et al.* (2002) 'Further evaluation of the Re-Os geochronometer in organic-rich sedimentary rocks: A test of hydrocarbon maturation effects in the Exshaw Formation, Western Canada Sedimentary Basin', *Geochimica et Cosmochimica Acta*, 66(19), pp. 3441–3452. doi: 10.1016/S0016-7037(02)00939-0.
- Davies, A. J. and John, C. M. (2017) 'Reducing contamination parameters for clumped isotope analysis: The effect of lowering Porapak™ Q trap temperature to below –50°C', *Rapid Communications in Mass Spectrometry*, 31(16), pp. 1313–1323. doi: 10.1002/rcm.7902.
- Defliese, W. F., Hren, M. T. and Lohmann, K. C. (2015) 'Compositional and temperature effects of phosphoric acid fractionation on δ^{47} analysis and implications for discrepant calibrations', *Chemical Geology*, 396, pp. 51–60. doi: 10.1016/j.chemgeo.2014.12.018.
- Dennis, K. J. (2011) *Clumped isotope paleothermometry and its application to Earth's history*. Harvard.
- Donnelly, T. H. and Crick, I. H. (1988) 'Depositional environment of the middle proterozoic velkerri formation in Northern Australia: Geochemical evidence', *Precambrian Research*, 42(1–2), pp. 165–172. doi: 10.1016/0301-9268(88)90015-0.
- Donnelly, T. H. and Jackson, M. J. (1988) 'Sedimentology and geochemistry of a mid-Proterozoic lacustrine unit from northern Australia', *Sedimentary Geology*, 58, pp. 145–169.
- Eiler, J. M. (2011) 'Paleoclimate reconstruction using carbonate clumped isotope thermometry', *Quaternary Science Reviews*. Elsevier Ltd, 30(25–26), pp. 3575–3588. doi: 10.1016/j.quascirev.2011.09.001.
- Eldridge, C. S., Williams, N. and Walshe, J. L. (1993) 'Sulfur isotope variability in sediment-hosted massive sulfide deposits as determined using the ion microprobe SHRIMP: II. A study of the H.Y.C. deposit at McArthur River, Northern Territory, Australia', *Economic Geology*, 88(1), pp. 1–26. doi: 10.2113/gsecongeo.88.1.1.
- Farquhar, J., Bao, H. and Thiemens, M. (2000) 'Atmospheric Influence of Earth's Earliest Sulfur Cycle', *Science*, 289(August), pp. 757–758. doi: 10.1126/science.289.5480.756.
- Flannery, E. N. and George, S. C. (2014) 'Assessing the syngeneity and indigeneity of hydrocarbons in the ~1.4 Ga Velkerri Formation, McArthur Basin, using slice experiments', *Organic Geochemistry*. Elsevier Ltd, 77(1), pp. 115–125. doi: 10.1016/j.orggeochem.2014.10.008.

- Garven, G. *et al.* (2001) 'Hydrothermal fluid flow models of stratiform ore genesis in the McArthur Basin, Northern Territory, Australia', *Geofluids*, 1, pp. 289–311. doi: 10.1046/j.1468-8123.2001.00021.x.
- George, S. C. and Ahmed, M. (2002) 'Use of aromatic compound distributions to evaluate organic maturity of the Proterozoic middle Velkerri Formation, McArthur Basin, Australia', *The sedimentary basins of Western Australia 3*; 3 : Procee(2002), pp. 253–270. doi: 10.1007/s13398-014-0173-7.2.
- Habicht, K. S. and Canfield, D. E. (1997) 'Sulfur isotope fractionation during bacterial sulfate reduction in organic-rich sediments', *Geochimica et Cosmochimica Acta*. Elsevier Science Ltd., 61(24), pp. 5351–5361. doi: 10.1016/S0016-7037(97)00311-6.
- Hannah, J. L. *et al.* (2004) 'Primitive Os and 2316 Ma age for marine shale: Implications for Paleoproterozoic glacial events and the rise of atmospheric oxygen', *Earth and Planetary Science Letters*, 225(1–2), pp. 43–52. doi: 10.1016/j.epsl.2004.06.013.
- Holland, H. D. (1984) *The Chemical Evolution of the Atmosphere and Oceans*. Princeton University Press.
- Holland, H. D. (2006) 'The Oxygenation of the aAtmosphere and Oceans', *Philosophical transactions of the Royal Society of London. Series B, Biological sciences*, 361(1470), pp. 903–915. doi: 10.1098/rstb.2006.1838.
- Holland, H. D. and Beukes, N. J. (1990) 'A paleoweathering profile from Griqualand West, South Africa: evidence for a dramatic rise in atmospheric oxygen between 2.2 and 1.9 bybp'.
- J. E. Gillott *et al.* (2002) 'Sedimentology and carbon-sulphur geochemistry of the Velkerri Formation, a mid-Proterozoic potential oil source in northern Australia', *Geochimica et Cosmochimica Acta*. Elsevier Ltd, 54(1), pp. 81–108. doi: 10.1038/nature02260.
- Jackson, M. J. *et al.* (1986) 'Hydrocarbon shows and petroleum source rocks in sediments as old as 1.7 × 10⁹ years', *Nature*, 322(6081), pp. 727–729. doi: 10.1038/322727a0.
- Jackson, M. J. *et al.* (1987) 'Geology of the southern McArthur Basin, Northern Territory (Australia).', *Bulletin - Bureau of Mineral Resources, Geology & Geophysics, Australia*, 220. Available at: <http://www.scopus.com/inward/record.url?eid=2-s2.0-0023509362&partnerID=40&md5=6020b8da4b3a6822ae2ad18b11739fdc%5Cnhttp://www.scopus.com/inward/record.url?eid=2-s2.0-0023509362&partnerID=tZ0tx3y1>.
- Jackson, M. J. and Raiswell, R. (1991) 'Sedimentology and carbon-sulphur geochemistry of the Velkerri Formation, a mid-Proterozoic potential oil source in northern Australia', *Precambrian Research*, 54(1), pp. 81–108.
- Jebrak, M. (1997) 'Hydrothermal breccias in vein-type ore deposits : A review of mechanisms , morphology and size distribution', pp. 111–134.
- Jenkyns, H. C., Lyons, T. W. and Severmann, S. (2006) 'DONALD E . CANFIELD The Iron Biogeochemical Cycle Past and Present', *Geochemistry, Geophysics, Geosystems*, 11(3), pp. 5698–5722. doi: 10.1029/2009GC002788.
- Kah, L. C., Lyons, T. W. and Frank, T. D. (2004) 'Low marine sulphate and protracted oxygenation of the Proterozoic biosphere', *Nature*, 431(7010), pp. 834–838. doi: 10.1038/nature02974.
- Kendall, B. *et al.* (2009) 'Re-Os and Mo isotope systematics of black shales from the Middle Proterozoic Velkerri and Wollongorang Formations, McArthur Basin, northern Australia', *Geochimica et Cosmochimica Acta*. Elsevier Ltd, 73(9), pp. 2534–2558. doi: 10.1016/j.gca.2009.02.013.
- Kralik, M. (1982) 'Rb-Sb age determinations on Precambrian carbonate rocks of the Carpentarian McArthur basin, Northern Territories, Australia', *Precambrian Research*, 18(1–2), pp. 157–170. doi: 10.1016/0301-9268(82)90044-4.
- Lynton S. Land (1980) 'THE ISOTOPIC AND TRACE ELEMENT GEOCHEMISTRY OF DOLOMITE THE Fairbridge Ingerson secondary in the synthesized All these examples only between poorly grade hydrothermal ore

deposits strictly nobody platform episodes Large and significant Mg carbonates havin', (November).

Lyons, T. W., Reinhard, C. T. and Planavsky, N. J. (2014) 'The rise of oxygen in Earth's early ocean and atmosphere', *Nature*. Nature Publishing Group, 506(7488), pp. 307–315. doi: 10.1038/nature13068.

Lyons, T. W. and Severmann, S. (2006) 'A critical look at iron paleoredox proxies: New insights from modern euxinic marine basins', *Geochimica et Cosmochimica Acta*, 70(23 SPEC. ISS.), pp. 5698–5722. doi: 10.1016/j.gca.2006.08.021.

Des Marais, D. J. *et al.* (1992) 'Carbon Isotope evidence for the stepwise oxidation of the Proterozoic environment', *Nature*, 359. doi: 10.1038/320129a0.

McDougall, I. *et al.* (1965) 'Isotopic age determinations on precambrian rocks of the carpentaria region, northern territory, Australia', *Journal of the Geological Society of Australia*, 12(1), pp. 67–90. doi: 10.1080/00167616508728586.

Milliken, K. L. *et al.* (2014) 'Sem Petrography of Eastern Mediterranean Sapropels: Analogue Data For Assessing Organic Matter In Oil and Gas Shales', *Journal of Sedimentary Research*, 84(11), pp. 961–974. doi: 10.2110/jsr.2014.75.

Muir, M. D. *et al.* (1985) 'Stable isotope, petrological, and fluid inclusion studies of minor mineral deposits from the McArthur Basin: Implications for the genesis of some sediment-hosted base metal mineralization from the Northern Territory', *Australian Journal of Earth Sciences*, 32(3), pp. 239–260. doi: 10.1080/08120098508729328.

Murray, S. T., Arienzo, M. M. and Swart, P. K. (2016) 'Determining the $\Delta 47$ acid fractionation in dolomites', *Geochimica et Cosmochimica Acta*. Elsevier Ltd, 174, pp. 42–53. doi: 10.1016/j.gca.2015.10.029.

Parnell, J. *et al.* (2004) 'Kaolin polytype evidence for a hot-fluid pulse along Caledonian thrusts during rifting of the European Margin', *Mineralogical Magazine*, 68(3), pp. 419–432. doi: 10.1180/0026461046830195.

Perkins, W. G. (1984) 'Mount Isa silica dolomite and copper orebodies: the result of a syntectonic hydrothermal alteration system.', *Economic Geology*, 79(4), pp. 601–637. doi: 10.2113/gsecongeo.79.4.601.

Petersen, S. V. *et al.* (2016) 'The effects of Porapak™ trap temperature on $\delta 18\text{O}$, $\delta 13\text{C}$, and $\Delta 47$ values in preparing samples for clumped isotope analysis', *Rapid Communications in Mass Spectrometry*, 30(1), pp. 199–208. doi: 10.1002/rcm.7438.

Poulton, S. W., Fralick, P. W. and Canfield, D. E. (2004) 'The transition to a sulphidic ocean , 1 . 84 billion years ago', *Nature*, 431(September), pp. 173–177. doi: 10.1038/nature02863.1.

Poulton, S. W., Fralick, P. W. and Canfield, D. E. (2010) 'Spatial variability in oceanic redox structure 1.8 billion years ago', *Nature Geoscience*. Nature Publishing Group, 3(7), pp. 486–490. doi: 10.1038/ngeo889.

Powell, T. G. and Jackson, M. J. (1987) 'BUREAU OF MINERAL RESOURCES , GEOLOGY AND GEOPHYSICS BY'.

Raiswell, R. *et al.* (1988) 'Degree of Pyritization of Iron as a Paleoenvironmental indicator of bottom-water oxygenation', 5(5).

Raiswell, R. and Berner, R. A. (1986) 'Pyrite and organic matter in Phanerozoic normal marine shales', *Geochimica et Cosmochimica Acta*, 50(9), pp. 1967–1976. doi: 10.1016/0016-7037(86)90252-8.

Raiswell, R. and Canfield, D. E. (1998) 'Sources of iron for pyrite formation in marine sediments.pdf', *American Journal of Science*, 298(March), pp. 219–245.

Ravizza, G. and Esser, B. K. (1993) 'A possible link between the seawater osmium isotope record and weathering of ancient sedimentary organic matter', *Chemical Geology*, 107(3–4), pp. 255–258. doi: 10.1016/0009-2541(93)90186-M.

Ravizza, G. and Turekian, K. K. (1989) 'Application of the 187Re - 187Os system to black shale geochronometry', *Geochimica et Cosmochimica Acta*, 53, pp. 3257–3262.

- Rawlings, D. J. (1999) 'Stratigraphic resolution of a multiphase intracratonic basin system: The McArthur Basin, northern Australia', *Australian Journal of Earth Sciences*, 46(5), pp. 703–723. doi: 10.1046/j.1440-0952.1999.00739.x.
- Revie, D. (2017) *Unconventional petroleum resources of the Roper Group, McArthur Basin*.
- Rye, D. M. and Williams, N. (1981) 'Studies of the base metal sulfide deposits at McArthur River, northern territory, Australia: III. the stable isotope geochemistry of the H.Y.C., ridge, and Cooley deposits', *Economic Geology*, 76(1), pp. 1–26. doi: 10.2113/gsecongeo.76.1.1.
- Shanks, W. C. and Bischoff, J. L. (1980) 'Geochemistry, sulfur isotope composition, and accumulation rates of Red Sea geothermal deposits', *Economic Geology*, 75(3), pp. 445–459. doi: 10.2113/gsecongeo.75.3.445.
- Shen, Y., Canfield, D. E. D. E. and Knoll, A. H. (2002) 'Middle Proterozoic Ocean Chemistry: Evidence from the McArthur Basin, Northern Australia', *American Journal of Science*, 302(January), pp. 1–27. doi: 10.1126/science.3.53.32.
- Shen, Y., Knoll, A. H. and Walter, M. R. (2003) 'Evidence for low sulphate and anoxia in a mid-Proterozoic marine basin', *Nature*, 423(6940), pp. 628–632. doi: 10.1038/nature01663.
- Shirey, S. B. and Walker, R. J. (1995) 'Carius tube digestion for low-blank rhenium-osmium analysis', *Analytical Chemistry*, 67(13), pp. 2136–2141.
- Spinks, S. C. *et al.* (2016) 'Evidence for SEDEX-style mineralization in the 1.7 Ga Tawallah Group, McArthur Basin, Australia', *Ore Geology Reviews*. Elsevier B.V., 76, pp. 122–139. doi: 10.1016/j.oregeorev.2016.01.007.
- Stein, H. J. (1997) 'and Accurate Ages for Molybdenite from the East Qinling Molybdenum ' h c g ' values for Y ''', *Geology*, 9(October).
- Stein, H. J. *et al.* (1998) 'Re-Os ages for Archean molybdenite and pyrite, Kuittila-Kivisuo, Finland and Proterozoic molybdenite, Kabeliai, Lithuania: Testing the chronometer in a metamorphic and metasomatic setting', *Mineralium Deposita*, 33(4), pp. 329–345. doi: 10.1007/s001260050153.
- Strauss, H. and Schieber, J. (1990) 'A sulfur isotope study of pyrite genesis: The mid-proterozoic Newland formation, belt supergroup, Montana', *Geochimica et Cosmochimica Acta*, 54(1), pp. 197–204. doi: 10.1016/0016-7037(90)90207-2.
- Summons, R. E., Taylor, D. and Boreham, C. J. (1994) 'Geochemical tools for evaluating petroleum generation in the Middle Proterozoic sediments of the McArthur Basin, Northern Territory, Australia', *Australian Petroleum Exploration Association Journal*, 34(1), pp. 692–707.
- Sweet, I. P. and Jackson, M. J. (1986) *BMR Stratigraphic Drilling in the Roper group, Northern Territory*.
- Tribovillard, N. *et al.* (2003) 'The geochemistry of rhenium and osmium in recent sediments from the Black Sea', *Geochimica et Cosmochimica Acta*. Elsevier B.V., 34(3–4), pp. 1099–1102. doi: 10.1016/0016-7037(90)90149-F.
- Warren, J. K. *et al.* (1998) 'Proterozoic source rocks: sedimentology and organic characteristics of the Velkerri Formation, Northern Territory, Australia', *AAPG Bulletin*, 82(3), pp. 442–463. doi: 10.1306/1D9BC435-172D-11D7-8645000102C1865D.
- Wilkin, R. T. and Barnes, H. L. (1997) 'Formation processes of framboidal pyrite', *Geochimica et Cosmochimica Acta*, 61(2), pp. 323–339. doi: 10.1016/S0016-7037(96)00320-1.
- Wilkin, R. T., Barnes, H. L. and Brantley, S. L. (1996) 'The size distribution of framboidal pyrite in modern sediments: An indicator of redox conditions', *Geochimica et Cosmochimica Acta*, 60(20), pp. 3897–3912. doi: 10.1016/0016-7037(96)00209-8.
- Williams, N. (1978) 'Studies of the Base Metal Sulfide Deposits at McArthur River, Northern Territory,

Australia: I. The Cooley and Ridge Deposits', *Economic Geology**Geology*, 73(6), pp. 1005–1035.

Supplementary Data

Table 2: The calculated mineral area percentage for samples 210.65m, 326.2m, and 151.58m. Total sample mineralogy is controlled by the influence of diagenetic vs detrital minerals.

Sample Depth	210.61m	Sample Depth	326.2m	Sample Depth	151.58m
Mineral	Measurement (Area%)	Mineral	Measurement (Area%)	Mineral	Measurement (Area%)
<i>Quartz</i>	43.14%	<i>Quartz</i>	38.52%	<i>Quartz</i>	4.19%
<i>Alkali Feldspar</i>	2.66%	<i>Alkali Feldspar</i>	1.89%	<i>Alkali Feldspar</i>	1.03%
<i>Dickite</i>	0.00%	<i>Dickite</i>	8.00%	<i>Dickite</i>	5.54%
<i>Illite</i>	19.54%	<i>Illite</i>	46.25%	<i>Illite</i>	8.93%
<i>Chlorite</i>	9.14%	<i>Chlorite</i>	0.00%	<i>Chlorite</i>	0.34%
<i>Smectites*</i>	4.93%	<i>Smectites*</i>	3.04%	<i>Smectites*</i>	3.31%
<i>Siderite</i>	0.00%	<i>Siderite</i>	0.00%	<i>Siderite</i>	0.00%
<i>Dolomite</i>	8.65%	<i>Dolomite</i>	0.00%	<i>Dolomite</i>	27.47%
<i>Ankerite</i>	6.73%	<i>Ankerite</i>	0.00%	<i>Ankerite</i>	10.13%
<i>Apatite</i>	1.11%	<i>Apatite</i>	0.04%	<i>Apatite</i>	0.33%
<i>Pyrite</i>	3.23%	<i>Pyrite</i>	0.95%	<i>Pyrite</i>	38.40%
<i>Sphalerite</i>	0.01%	<i>Sphalerite</i>	0.01%	<i>Sphalerite</i>	0.00%
<i>Chalcopyrite*</i>	0.16%	<i>Chalcopyrite*</i>	0.02%	<i>Chalcopyrite*</i>	0.01%
<i>Magnesioferrite*</i>	0.00%	<i>Magnesioferrite*</i>	0.53%	<i>Magnesioferrite*</i>	0.11%
<i>Goethite</i>	0.47%	<i>Goethite</i>	0.37%	<i>Goethite</i>	0.03%
<i>Rutile</i>	0.20%	<i>Rutile</i>	0.34%	<i>Rutile</i>	0.14%
<i>Unclassified</i>	0.03%	<i>Unclassified</i>	0.05%	<i>Unclassified</i>	0.02%

Table 3: Raw stable and clumped isotope data

Sample #	C00445	C00446	C00469	C00458
Sample ID	U4 210.65_75	U4 146.76_86 Urapunga	Urapunga 4 161.25	Urapunga 4 142.2
Date	23-05-18	23-05-18	15-06-18	06-06-18
CC	8	3	8	8
$\delta^{13}\text{C}$ (VPDB)	-9.034505807	-10.18291113	-10.67680964	-3.473275961
Std. Dev.	0.019936343	0.019980693	0.019123315	0.024103378
Std. Er.	0.002664106	0.004360145	0.00255546	0.003220949
$\delta^{18}\text{O}$ (VPDB)	-12.92123081	-13.16832148	-12.84624455	-11.82177343
d18O (dolomite)	-13.72123081	-13.96832148	-13.64624455	-12.62177343
Std. Dev.	0.033742734	0.034763799	0.075271049	0.042996496
Std. Er.	0.004509062	0.007586083	0.010058517	0.005745648
$\delta 45$	-2.303615007	-3.393058412	-3.846719018	2.967067524
Std. Dev.	0.019983828	0.019952129	0.019528862	0.024345986
Std. Er.	0.002694619	0.004353911	0.002633271	0.003282812
$\delta 46$	-1.077753298	-1.330696034	-1.005954448	0.047495278
Std. Dev.	0.0345155	0.035259477	0.07688472	0.043969155
Std. Er.	0.004654069	0.007694249	0.010367134	0.0059288
$\delta 47$	-3.885740856	-5.230999147	-5.454101236	2.641463067
Std. Dev.	0.080874859	0.090375202	0.081748947	0.075597706
Std. Er.	0.010905164	0.019721486	0.011023026	0.010193593
$\delta 48$	164.4132983	754.7380563	7.892189907	15.67374666
Std. Dev.	8.342071433	25.54322889	0.416222463	0.502779236
Std. Er.	1.124844683	5.573989519	0.056123425	0.067794738
$\delta 49$	-12.98632876	-138.0345754	19.40310807	-7.749548785
Std. Dev.	4.556006772	5.347877928	6.209605775	6.212085223
Std. Er.	0.614331828	1.167002639	0.837303072	0.837637401
$\Delta 47$	-0.454804931	-0.429204535	-0.504676821	-0.463464837
Std. Dev.	0.05892363	0.07537368	0.105328723	0.055253962
Std. Er.	0.007874001	0.016447886	0.014075143	0.007383621
$\Delta 48$	166.6583619	759.4173191	9.918120459	15.56458414
Std. Dev.	8.477228433	25.60556116	0.491345816	0.535087015
Std. Er.	1.1328173	5.587591536	0.065658847	0.07150401
$\Delta 49$	-8.469293696	-132.6409027	25.74644722	-10.91273142
Std. Dev.	4.459422961	5.307851693	6.149936048	6.044081548
Std. Er.	0.595915459	1.158268198	0.821819773	0.80767437
Temperature of Reaction	90	90	90	90
49 Parameter	-0.859643248	-8.122091884	1.03181037	-0.527130037

Sample #	C00472	C00486	C00454	C00474
Sample ID	Urapunga 4 142.2	Urapunga 4 142.2	Urapunga 4 152.4m	Urapunga 4 152.4m
Date	18-06-18	27-06-18	04-06-18	19-06-18
CC	8	8	5	8
$\delta^{13}\text{C}$ (VPDB)	-6.50176	-6.01429	-6.85511	-7.25801
Std. Dev.	0.013404	0.00884	0.014757	0.020059
Std. Er.	0.001791	0.001181	0.002494	0.00268
$\delta^{18}\text{O}$ (VPDB)	-11.703	-12.0399	-11.9828	-11.9713
d18O (dolomite)	-12.503	-12.8399	-12.7828	-12.7713
Std. Dev.	0.0238	0.020725	0.025162	0.039993
Std. Er.	0.00318	0.002769	0.004253	0.005344
$\delta 45$	0.121846	0.740496	-0.22041	-0.5993
Std. Dev.	0.013524	0.008582	0.014735	0.020339
Std. Er.	0.001824	0.001157	0.002491	0.002743
$\delta 46$	0.161568	0.093027	-0.12255	-0.11221
Std. Dev.	0.02436	0.02111	0.025522	0.040812
Std. Er.	0.003285	0.002847	0.004314	0.005503
$\delta 47$	-0.25682	0.387554	-0.8172	-1.25875
Std. Dev.	0.061314	0.097528	0.075884	0.082984
Std. Er.	0.008268	0.013151	0.012827	0.01119
$\delta 48$	39.41502	64.86128	0.28073	0.512361
Std. Dev.	1.271188	0.900572	0.251704	0.231394
Std. Er.	0.171407	0.121433	0.042546	0.031201
$\delta 49$	-1.26676	-32.0074	0.760266	-10.5022
Std. Dev.	2.230749	18.79323	3.10761	3.048731
Std. Er.	0.300794	2.534079	0.525282	0.411091
$\Delta 47$	-0.5422	-0.46892	-0.46953	-0.53047
Std. Dev.	0.048155	0.102735	0.061475	0.055056
Std. Er.	0.006435	0.013729	0.010391	0.007357
$\Delta 48$	39.04338	64.64164	0.525947	0.743998
Std. Dev.	1.296116	0.914097	0.250694	0.245612
Std. Er.	0.173201	0.122151	0.042375	0.032821
$\Delta 49$	-1.6674	-32.784	1.236298	-9.63916
Std. Dev.	2.182592	18.61602	3.053705	2.935251
Std. Er.	0.291661	2.48767	0.51617	0.392239
Temperature of Reaction	90	90	90	90
49 Parameter	-0.05772	-2.09398	0.051261	-0.51125

Sample #	C00477	C00456	C00491	C00460
Sample ID	Urapunga 4 152.4	Urapunga 155.7	Urapunga 4 155.7	Urapunga 4 158.53
Date	21-06-18	05-06-18	29-06-18	07-06-18
CC	8	8	8	8
$\delta^{13}\text{C}$ (VPDB)	-5.61346104	-10.54733713	-10.68619872	-4.559186125
Std. Dev.	0.01240324	0.009710825	0.008118066	0.020268933
Std. Er.	0.001657453	0.001297664	0.001084822	0.00270855
$\delta^{18}\text{O}$ (VPDB)	-11.82045733	-13.00311074	-13.23158837	-11.63076107
d18O (dolomite)	-12.62045733	-13.80311074	-14.03158837	-12.43076107
Std. Dev.	0.023564896	0.015208284	0.011650017	0.036191286
Std. Er.	0.003148992	0.002032292	0.001556799	0.004836264
$\delta 45$	0.953660161	-3.730188462	-3.697676164	1.952136524
Std. Dev.	0.012529743	0.009668479	0.007831459	0.02048062
Std. Er.	0.00168951	0.001303697	0.001055994	0.002761606
$\delta 46$	0.044594066	-1.164120119	-1.124114544	0.239045028
Std. Dev.	0.024115466	0.015565509	0.011871916	0.037040599
Std. Er.	0.003251729	0.002098853	0.001600809	0.004994553
$\delta 47$	0.490154881	-5.508083229	-5.404608605	1.809899079
Std. Dev.	0.056979718	0.047758857	0.08554291	0.084837211
Std. Er.	0.007683144	0.006439803	0.011534604	0.011439447
$\delta 48$	-0.110314032	564.0863528	157.8696718	711.2779411
Std. Dev.	0.206430997	22.20747069	2.255982061	20.84678783
Std. Er.	0.02783515	2.994454738	0.304196559	2.810980298
$\delta 49$	6.283887521	-78.13631542	-30.13874888	-98.6221205
Std. Dev.	2.03520825	3.460599253	13.5851601	5.597725025
Std. Er.	0.274427424	0.466627108	1.831822614	0.754797088
$\Delta 47$	-0.536272197	-0.521348987	-0.49091313	-0.437164386
Std. Dev.	0.055949461	0.047054246	0.08469053	0.067453066
Std. Er.	0.007476561	0.006287888	0.011317248	0.009013795
$\Delta 48$	-0.191405224	567.0134957	160.402092	709.7652619
Std. Dev.	0.203522166	22.71539067	2.319051822	21.29184772
Std. Er.	0.027196793	3.035471761	0.309896335	2.845242832
$\Delta 49$	5.153675218	-72.31895448	-24.12068627	-100.8574862
Std. Dev.	1.96820917	3.432193874	13.5399659	5.472034019
Std. Er.	0.263013014	0.458646199	1.80935405	0.731231304
Temperature of Reaction	90	90	90	90
49 Parameter	0.306507852	-4.991393483	-1.950830302	-6.155800749

Sample #	C00498	C00470	C00493	C00495
Sample ID	Urapunga 4 158.53	Urapunga 4 225.57	Urapunga 4 225.57	Urapunga 4 225.57
Date	05-07-18	15-06-18	02-07-18	03-07-18
CC	8	8	8	8
$\delta^{13}\text{C}$ (VPDB)	-2.528329201	-7.33474536	-10.8867819	-10.68457362
Std. Dev.	0.005506809	0.017777816	0.017078606	0.004302492
Std. Er.	0.000735878	0.002375661	0.002282225	0.000574945
$\delta^{18}\text{O}$ (VPDB)	-11.53925113	-12.19730924	-13.40993523	-13.33974656
d18O (dolomite)	-12.33925113	-12.99730924	-14.20993523	-14.13974656
Std. Dev.	0.008929231	0.064131128	0.023755153	0.007592528
Std. Er.	0.001193219	0.008569882	0.003174416	0.001014594
$\delta 45$	3.866085655	-0.679490405	-3.892577458	-3.699949142
Std. Dev.	0.005153869	0.018526184	0.016961192	0.004061125
Std. Er.	0.000694948	0.00249807	0.002287047	0.000547602
$\delta 46$	0.335900123	-0.340332743	-1.305480785	-1.234137385
Std. Dev.	0.009105465	0.065455333	0.024322188	0.007473912
Std. Er.	0.001227781	0.008825995	0.003279603	0.001007782
$\delta 47$	3.848086635	-1.585612678	-5.938657855	-5.62611658
Std. Dev.	0.068249461	0.080961389	0.098833361	0.053257354
Std. Er.	0.009202755	0.010916831	0.013326688	0.00718122
$\delta 48$	0.92845463	314.5128878	-0.701088328	-2.155515536
Std. Dev.	0.401696799	4.937411092	0.432979134	0.306016882
Std. Er.	0.054164785	0.665760376	0.058382895	0.041263308
$\delta 49$	-9.113088197	-14.35457697	25.91088343	-1.472578673
Std. Dev.	8.609285656	6.142453036	10.0351311	3.240251545
Std. Er.	1.160875841	0.828248198	1.353136801	0.436915429
$\Delta 47$	-0.470658383	-0.551122814	-0.64996433	-0.604767839
Std. Dev.	0.066870657	0.077355811	0.085765069	0.055218978
Std. Er.	0.008935967	0.010337105	0.011460839	0.007378946
$\Delta 48$	0.267554251	315.2856719	1.906949734	0.303643973
Std. Dev.	0.414607042	5.010376108	0.422175913	0.312951597
Std. Er.	0.055404196	0.669539671	0.056415629	0.041819916
$\Delta 49$	-14.00592034	-12.86748049	32.99979388	4.936113331
Std. Dev.	8.587551084	6.03514911	10.12472456	3.229658853
Std. Er.	1.147559784	0.806480723	1.35297323	0.431581318
Temperature of Reaction	90	90	90	90
49 Parameter	-0.619128572	-0.758418124	2.066902973	-0.090028768

Sample #	C00479	C00465
Sample ID	Urapunga 4 377.47	Urapunga 4 377.47
Date	22-06-18	13-06-18
CC	8	8
$\delta^{13}\text{C}$ (VPDB)	-38.29877066	-38.61028217
Std. Dev.	0.023930022	0.018905803
Std. Er.	0.003197784	0.002572754
$\delta^{18}\text{O}$ (VPDB)	-8.551158268	-8.489377966
d18O (dolomite)	-9.351158268	-9.289377966
Std. Dev.	0.049972709	0.128244
Std. Er.	0.006677884	0.017451798
δ^{45}	-29.68567166	-29.97753046
Std. Dev.	0.02420269	0.017784738
Std. Er.	0.00326349	0.002398094
δ^{46}	3.288394871	3.320591486
Std. Dev.	0.050276459	0.203132863
Std. Er.	0.006779276	0.02739043
δ^{47}	-28.02379479	-28.24679838
Std. Dev.	0.099784753	0.066623336
Std. Er.	0.013454973	0.008983489
δ^{48}	7.176384007	8.541620919
Std. Dev.	0.27008995	0.250907482
Std. Er.	0.036418921	0.033832358
δ^{49}	9.245567209	-8.584236282
Std. Dev.	4.712992155	4.412210369
Std. Er.	0.635499732	0.594942325
Δ^{47}	-0.547033358	-0.52604318
Std. Dev.	0.073426628	0.139019887
Std. Er.	0.009812046	0.01891821
Δ^{48}	0.587131288	1.82380999
Std. Dev.	0.251162069	0.362155877
Std. Er.	0.033562943	0.049283173
Δ^{49}	35.37914754	17.46150038
Std. Dev.	4.777004473	4.450359439
Std. Er.	0.638354074	0.605617211
Temperature of Reaction	90	90
49 Parameter	0.447894787	

Table : Empirical transfer function data. Temperature of reaction and diagnostics for ThermoFisher MAT 253-plus mass spectrometer.

Dennis et al	2011	Empirical	Transfer
Days since last Heated Gas Ran	36	36	17
Days since last 25C Water	98	98	16
Days Since Last 50C Water	79	79	102
Days Since Last 90C Water Ran	23	23	2
Heated Slope	0.000353224	0.000353224	0.002968568
25C Slope	0.000548098	0.000548098	0.001839574
50C Slope	0.002797113	0.002797113	0.003611462
90C Slope	0.004252203	0.004252203	0.001336418
Slope Average	0.001987659	0.001987659	0.002439005
Heated Intercept	-0.830910999	-0.830910999	-0.904228661
25C Intercept	0.061570713	0.061570713	0.020850338
50C Intercept	-0.151987879	-0.151987879	-0.172476909
90C Intercept	-0.242272392	-0.242272392	-0.221419765
Heated Reference	0.026614442	0.026614442	0.026614442
25C Reference	0.924413375	0.924413375	0.924413375
50C Reference	0.804292059	0.804292059	0.804292059
90C Reference	0.650975135	0.650975135	0.650975135
ETF Slope	1.039609407	1.039609407	0.983111797
ETF Intercept	0.903996274	0.903996274	0.915499782
$\Delta 47$ -[SGvsWG]0	-0.447081401	-0.41880709	-0.491374239
$\Delta 47$ -RF	0.439206244	0.468600484	0.43242397
$\Delta 47$ -AC	0.522958096	0.552352336	0.516175823
Temp. (Eq. 9)	74.02804621	64.74406051	76.28102171
Temp. (Eq. 10)	122.7519947	99.73382569	128.6962307
Kelson et al. (2016) (90C reactions)	104.776866	87.07785883	109.244534
Bonifacie et al. (2016) (90C Reactions/Dolomite)	97.08514248	80.94049902	101.1343883
Defliese et al. (2015)	116.4446294	94.9505612	121.9619247
Miami SIL	106.2002124	87.60448274	110.9148062
Temperature (K)	370.2351425	354.090499	374.2843883
Calcite Oxygen (SMOW)	16.76464595	16.5099177	16.84195003
Alpha K&O'N (1997)	1.016412002	1.018671356	1.015876642
Water K&O'N (1997)	0.346949874	-2.121821052	0.950221746
Alpha M&K(1977)	1.019266956	1.021391375	1.018777407
Water M&K(1977)	-2.455009624	-4.77922273	-1.89978362

Function				
8	20	29	6	21
7	19	28	5	20
93	105	2	91	106
37	5	14	35	6
0.001396973	0.003492433	0.005064027	0.00104773	0.003667054
0.001199644	0.002052884	0.002692813	0.001057437	0.002123987
0.003292804	0.003717682	0.00394632	0.003221991	0.003753088
0.002192039	0.001598109	0.002383182	0.002486348	0.001685339
0.002020365	0.002715277	0.003521586	0.001953377	0.002807367
-0.865454716	-0.917153309	-0.955927254	-0.856838283	-0.921461525
0.047463582	0.011979257	-0.014633987	0.053377636	0.00902223
-0.164459462	-0.175149391	-0.18120286	-0.162677808	-0.176040219
-0.225575481	-0.227708874	-0.246576201	-0.227960754	-0.229805244
0.026614442	0.026614442	0.026614442	0.026614442	0.026614442
0.924413375	0.924413375	0.924413375	0.924413375	0.924413375
0.804292059	0.804292059	0.804292059	0.804292059	0.804292059
0.650975135	0.650975135	0.650975135	0.650975135	0.650975135
1.008780974	0.976482594	0.956002928	1.01450437	0.974266378
0.906232183	0.92089145	0.935778109	0.904428469	0.922663882
-0.468801556	-0.541507191	-0.470285537	-0.467933376	-0.526933443
0.433314093	0.392119104	0.486183759	0.429708015	0.409290345
0.517065946	0.475870956	0.569935611	0.513459867	0.493042197
75.98283318	90.63919651	59.53428728	77.19560315	84.30907519
127.9008043	170.5584686	87.74609888	131.1528173	151.1867776
108.6491412	139.5166655	77.60948738	111.078568	125.7668777
100.5953715	128.2866239	72.23721414	102.7935719	116.0160861
121.2244366	160.4131561	83.67738559	124.2379927	142.7093121
110.2860158	143.0914681	77.70796533	112.8526713	128.4255017
373.7453715	401.4366239	345.3872141	375.9435719	389.1660861
17.89808755	18.02048189	17.67320385	17.73209906	17.74391103
1.015947221	1.012572062	1.019979246	1.015660688	1.014007025
1.920243875	5.380772497	-2.260871429	2.039471258	3.685265993
1.018841643	1.015873018	1.022664292	1.018581433	1.017109373
-0.926106048	2.113909416	-4.880475282	-0.833839915	0.623864475

23	7	1	9	7
22	6	30	8	36
108	92	4	94	10
8	36	16	38	22
0.004016297	0.001222351	0.005267796	0.001571595	0.00544268
0.002266193	0.001128541	0.00283502	0.001270747	0.00326164
0.003823901	0.003257397	0.003927114	0.00332821	0.003869494
0.0018598	0.002339194	0.002557643	0.002044885	0.003081025
0.002991548	0.001986871	0.003646893	0.002053859	0.00391371
-0.930077957	-0.8611465	-0.959739213	-0.869762932	-0.956761671
0.003108176	0.050420609	-0.020548041	0.044506555	-0.038290203
-0.177821873	-0.163568635	-0.181020538	-0.16535029	-0.18047357
-0.233997983	-0.226768117	-0.250768941	-0.224382844	-0.263347159
0.026614442	0.026614442	0.026614442	0.026614442	0.026614442
0.924413375	0.924413375	0.924413375	0.924413375	0.924413375
0.804292059	0.804292059	0.804292059	0.804292059	0.804292059
0.650975135	0.650975135	0.650975135	0.650975135	0.650975135
0.969825486	1.011664119	0.956443429	1.005856325	0.973961218
0.926171831	0.905341748	0.939216631	0.907099974	0.951925281
-0.537738519	-0.510405137	-0.4712031	-0.440881664	-0.485718677
0.40465931	0.388983185	0.488537522	0.463636364	0.478854127
0.488411163	0.472735037	0.572289374	0.547388216	0.56260598
85.9836843	91.83197284	58.85501984	66.25975411	61.67654166
156.1601951	174.3912897	86.22757043	103.3403578	92.60105763
129.3393001	142.1847096	76.39785705	89.89284147	81.46479481
119.2142245	130.6554491	71.12020441	83.5191672	75.78650603
147.2694446	163.8972884	82.24559595	98.33164201	88.24935914
132.2276029	145.9474995	76.44405836	90.55357028	81.73337965
392.3642245	403.8054491	344.2702044	356.6691672	348.936506
17.89944433	16.68023511	16.44469523	18.09500411	18.18934262
1.013624176	1.01230531	1.020152018	1.018296413	1.019437793
4.217803842	4.321745084	-3.634089024	-0.197789857	-1.224645696
1.016775783	1.01564739	1.022834809	1.021032291	1.02213348
1.105121759	1.016932804	-6.247454777	-2.876781363	-3.858730578

17	4	5	24	15
16	33	34	23	14
102	7	8	109	100
2	19	20	9	0
0.002968568	0.005355238	0.005384385	0.004190919	0.002619324
0.001839574	0.00304833	0.003119433	0.002337297	0.001697367
0.003611462	0.003898304	0.003888701	0.003859308	0.003540649
0.001336418	0.002819334	0.002906564	0.00194703	0.001161957
0.002439005	0.003780301	0.003824771	0.003083638	0.002254824
-0.904228661	-0.958250442	-0.957754185	-0.934386173	-0.895612228
0.020850338	-0.029419122	-0.032376149	0.000151149	0.026764392
-0.172476909	-0.180747054	-0.180655893	-0.178712701	-0.170695254
-0.221419765	-0.25705805	-0.25915442	-0.236094353	-0.217227025
0.026614442	0.026614442	0.026614442	0.026614442	0.026614442
0.924413375	0.924413375	0.924413375	0.924413375	0.924413375
0.804292059	0.804292059	0.804292059	0.804292059	0.804292059
0.650975135	0.650975135	0.650975135	0.650975135	0.650975135
0.983111797	0.965195313	0.968116075	0.967601218	0.987512885
0.915499782	0.94553912	0.947660884	0.927907442	0.911842924
-0.547255496	-0.627514413	-0.583249233	-0.460618108	-0.462351609
0.377486448	0.33986515	0.383007926	0.4822128	0.455264752
0.4612383	0.423617002	0.466759779	0.565964652	0.539016605
96.30738518	112.191604	94.13757244	60.68976919	68.86272103
189.3427803	251.2929941	181.9779869	90.35217925	109.6669964
152.4280714	192.136785	147.4150412	79.6824639	94.79335408
139.7127962	174.2531585	135.2876001	74.14658431	87.99850637
177.4284284	232.4362456	170.7753011	86.13263985	104.2509097
156.9442991	200.0760002	151.5562047	79.87169217	95.6951411
412.8627962	447.4031585	408.4376001	347.2965843	361.1485064
17.51094393	16.26083567	16.33319387	21.26979743	21.33348736
1.011314209	1.007910347	1.011792823	1.019686556	1.017658155
6.127407935	8.284952286	4.487450668	1.552674968	3.611559213
1.014820632	1.012119895	1.015217611	1.022376681	1.020427009
2.651022131	4.091353413	1.098861094	-1.082657228	0.888332199